Linear instability, nonlinear instability, and ligament dynamics in three-dimensional laminar two-layer liquid/liquid flows

Lennon Ó Náraigh[1], Prashant Valluri[2], D. Scott[3], I. Bethune[3], and Peter D. M. Spelt[4]

[1]School of Mathematical Sciences, University College Dublin, Belfield, Dublin 4
[2]Institute of Materials and Processes, Sanderson Building, School of Engineering, University of Edinburgh, King's Buildings, Edinburgh, EH9 3JL, UK
[3]Edinburgh Parallel Computing Centre, The University of Edinburgh, United Kingdom
[4] Laboratoire de Mécanique des Fluides & d'Acoustique, CNRS, Ecole Centrale Lyon, Ecully, France, and Département de Mécanique, Université de Lyon 1, France

Abstract

We consider the linear and nonlinear stability of two-phase density-matched but viscosity-contrasted fluids subject to laminar Poiseuille flow in a channel, paying particular attention to the formation of three-dimensional waves. A combination of Orr–Sommerfeld–Squire analysis with direct numerical simulation of the three-dimensional two-phase Navier–Stokes equations is used. For the parameter regimes under consideration, under linear theory, the most unstable waves are two-dimensional. Nevertheless, we demonstrate the existence of two distinct mechanisms whereby three-dimensional waves enter the system, and dominate at late time. There exists a direct route, whereby three-dimensional waves are amplified by the standard linear mechanism; for certain parameter classes, such waves grow at a rate less than but comparable to that of most-dangerous two-dimensional mode. Additionally, there is a weakly nonlinear route, whereby a purely spanwise wave couples to a streamwise mode and grows exponentially. We demonstrate these mechanisms in isolation and in concert. Consideration is also given to the ultimate state of these waves: persistent three-dimensional nonlinear waves are stretched and distorted by the base flow, thereby producing regimes of ligaments, 'sheets', or 'interfacial turbulence'. Depending on the parameter regime, these regimes are observed either in isolation, or acting together.

1   Introduction

Two-layer channel flows are a useful model for several industrial systems, including oil/gas transport and the cleaning of surfaces by flow. A large body of literature is devoted to the linear theory of infinitesimally small perturbations in these flows, mostly on (periodic) two-dimensional perturbations in the streamwise and wall-normal directions of a uni-directional base state. The subject of this paper is the

route by which three-dimensional small-amplitude waves eventually lead to wave overturning, ligament formation and droplet entrainment allowing for flows that are not periodic in the main flow direction. We concentrate herein on density-matched laminar systems, representative of liquid/liquid flows, with the view that the additional effects of a density contrast is best studied subsequently; a viscosity contrast is anyway usually present in gas/liquid systems, and is known often to produce the dominant mechanism for linear instability, as recalled below. Our objective is accomplished using a high-resolution direct numerical simulation of two-phase density-matched but viscosity-contrasted flows in a long channel.

One possible route to droplet formation is a purely linear one: a single linear mode dominates and holds up to a very late stage before ligament formation. Prior work on linear stabililty analysis of two-layer channel flows has been mostly on two-dimensional systems, within the framework of Orr–Sommerfeld theory. Results obtained with two-dimensional nonlinear direct numerical simulations in Valluri *et al.* (2007, 2010) follow linear theory up to a point close to the turnover of waves. Linear stability analysis has revealed that the dominant mechanism that leads to linear temporal growth is the so-called Yih mechanism (Yiantsios & Higgins, 1988), due to the viscosity contrast across the interface (Yih, 1967). Viscosity stratification leads to net work being done by the perturbation velocity and stress at the interface. By using an energy budget, Boomkamp & Miesen (1996) verified that this mechanism plays an important role in many papers on interfacial instability. Other mechanisms for instability are also conveniently summarized by Boomkamp & Miesen (1996). Of particular importance for laminar two-layer flow here also is a Tollmien–Schlichting or shear-type mechanism (possibly in both fluids). Although the Yih mechanism usually dominates, its growth rate being rather large and shear modes only being unstable beyond a critical Reynolds number with relatively low growth rates, competition between these modes has been observed by particular choices of flow parameters (Yecko *et al.*, 2002). The extension of the modal analysis to three-dimensional disturbances, although not straightforward in view of the fact that Squire's theorem does not necessarily apply (Yiantsios & Higgins, 1988), shows that the dominant mode is two-dimensional in a wide range of multiphase flow situations, albeit that for some parameter values large-amplitude three-dimensional waves might result (Sahu & Matar, 2011).

In practice, disturbances are expected initially to be localized, and modal temporal stability analysis may be of restricted value, as the manner whereby such initially localized pulses are amplified should really be considered in linearly unstable cases: either amplification in at least one moving frame of reference and damping in the laboratory frame (convective instability), or growing disturbances in the entire domain in the laboratory frame (absolute instability). To determine absolute instability from the Orr–Sommerfeld theory for the two-dimensional model, the saddle-point method was used initially in Valluri *et al.* (2010); Ó Náraigh *et al.* (2013) but difficulties arose due to the presence of singularities in the complex wavenumber plane and due to spatio-temporal mode competition. It was therefore necessary to confirm independently the boundaries between convectively and absolutely unstable cases in parameter space. For this purpose, an alternative approach was developed in by Ó Náraigh *et al.* (2013) wherein the Orr–Sommerfeld eigenvalue

problem was converted into a Cauchy problem such that highly-efficient DNS of the linearized equations of motion can be performed, and the evolution of an initially-localized pulse tracked (the so-called ray-analysis approach, based on earlier work on single-phase flows (Delbende & Chomaz, 1998; Delbende *et al.*, 1998)). Using this approach, the evolution of a pulse in an arbitrary frame of reference travelling at velocity v with respect to the laboratory frame can be tracked, and the pulse growth rate obtained as a function of v, from which the convectively or absolutely unstable nature of instability can then be concluded. The existing evidence (Sahu & Matar, 2011) is that allowing for three-dimensional disturbances does not significantly move convective/absolute boundaries here.

The extent to which such linear theory governs three-dimensional wave growth has not yet been established. Furthermore, the growth rates from a modal linear analysis are merely asymptotic (i.e. valid in the notional limit as $t \to \infty$ but before the onset of nonlinear effects). Effects not captured by a modal analysis can be present at early times and lead to substantial transient growth because the Orr–Sommerfeld equation is non-normal and the eigenfunctions of a given mode are not orthogonal. In this way, the growth of an arbitrarily-chosen initial condition containing a mixture of Orr–Sommerfeld eigenmodes can produce transient growth rates that are orders of magnitude in excess of the asymptotic growth rates computed from the standard eigenvalue analyses. Transient growth has been reported for the two-dimensional two-layer channel-flow problem (van Noorden *et al.*, 1998) and for transverse modes in a two-layer mixing layer (Yecko & Zaleski, 2005).

Various nonlinear mechanisms may eventually become dominant. For instance, the linearly-most-dangerous streamwise mode may interact weakly nonlinearly with spanwise modes, and the evolution of the spanwise modes is 'slaved' via a centre-manifold-type approximation to the streamwise spanwise mode. For generic references to this theory, see the work by Schmid & Henningson (2001). A specific version of this theory also exists, but concerns only streamwise (two-dimensional) modes in the context of a longwave model that only approximates the underlying equations of motion (Barthelet *et al.*, 1995). An extension of this approach has been carried out by King & McCready (2000), and accounts for a range of of weakly nonlinear interactions between a wide variety of modes that are strongly excited in the linear theory. The work by King & McCready (2000) is based on the full linearized Navier–Stokes equations, but is still focused only on streamwise (two-dimensional) modes.

The linearly-most-dangerous streamwise mode may stabilize at large amplitude and thereafter, a finite-amplitude unidirectional travelling wave superimposed on the base state is treated as a 'new' base state. This new base state may be unstable to three-dimensional perturbations. Typically, secondary growth rates are computed via Floquet analysis (Schmid & Henningson, 2001). For gas/liquid jet flows, such a route has been identified by Marmottant & Villermaux (2004), involving a secondary instability of Rayleigh-Taylor type. Although the present study is on density-matched systems, ligament growth is observed in the results below, such that there must be mechanisms other than the Rayleigh–Taylor instability at work here.

Once a wave has overturned to form a ligament, various scenarios may lead

to droplets. A tentative study of three-dimensional two-phase mixing-layer flow by Scardovelli & Zaleski (1999) found that initial conditions corresponding to two-dimensional linear theory cause the interface to develop into 'sheets', which break to form cylinders that subsequently break up due to capillary instability. On the other hand, for initial conditions that are sufficiently far from the description given by linear theory, spanwise waves were found to develop on the sheet edges that further develop into cylinders – this time pointing in the streamwise direction - which then break up. Sheets and ligaments are observed in jet breakup as well as in two-layer flows, with sheets often inflated resulting in a bag-type shape in gas/liquid systems (e.g. the work by Marmottant & Villermaux (2004)).

Various governing mechanisms of the evolution of three-dimensional sheets and ligaments have been identified. In the work by Marmottant & Villermaux (2004), a simple force balance was proposed as a model of ligament dynamics in gas-assisted jet breakup: mainly form drag exerted by the gas flow was argued to lead to an increase in momentum of the ligament. A different mechanism has been identified in breakup of droplets pinned on an adhering surface by shear flow in density-matched systems: there, the work done by the tangential stress exerted by the exterior fluid is converted into surface energy (Ding *et al.*, 2010).

This paper is organized as follows. After an overview of methodology and validation tests in Section 2, and an outline of the pertinent general behaviour of modal linear growth in Section 3, we use direct numerical simulations of channel flows in a periodic domain in Section 4 to establish to what extent linear theory is followed, or whether a non-linear mechanism becomes significant before the turnover of waves. In Section 5 we investigate whether the findings for periodic domains carry over to 'open' domains (with an inlet and an outlet). Ligament dynamics are investigated in Section 6. In Section 7, we report a transition to a highly-agitated flow regime. Concluding remarks are presented in Section 8.

2   Problem statement and computational methodologies

In this section we present the problem statement and the two computational methodologies used in this study, which are linear theory and direct numerical simulation (DNS) of the fully nonlinear governing equations.

2.1   Problem statement

Throughout this paper, we study the two-phase Navier–Stokes equations, in a rectangular Cartesian frame (x, y, z) in a channel geometry $[0, L_x] \times [0, L_y] \times [0, L_z]$. We fix $L_z = 1$ in the nondimensional framework described below. We are interested in density-matched pressure-driven channel flow, for which an equilibrium configuration is unidirectional two-phase Poiseuille flow, wherein the phases are confined in two layers parallel to the direction of flow. Either the pressure gradient or the flow rate is fixed. We therefore assign labels $j = B, T$ to the fluid layers, and consider the case in which the bottom layer contains the more viscous fluid. The dimensionless physical parameters in the problem are the Reynolds number $Re = \rho_T V L_z / \mu_T$, the viscosity ratio $m = \mu_B / \mu_T$ (bottom/top), the surface-tension parameter (inverse

capillary number) $\mathcal{S} = \gamma/(\mu_T V)$. Here, γ denotes the (dimensional) surface tension. Across interfaces separating the two phases, the following standard jump conditions are satisfied:

$$\llbracket \widehat{\boldsymbol{n}} \cdot \left[-p\mathbb{I} + \mu_j \left(\nabla \boldsymbol{u}_j + \nabla \boldsymbol{u}_j^T \right) \right] \rrbracket \cdot \widehat{\boldsymbol{t}}^{(r)} = 0, \qquad \llbracket \widehat{\boldsymbol{n}} \cdot \left[-p\mathbb{I} + \mu_j \left(\nabla \boldsymbol{u}_j + \nabla \boldsymbol{u}_j^T \right) \right] \cdot \widehat{\boldsymbol{n}} \rrbracket = \mathcal{S}\kappa, \tag{1}$$

where $\widehat{\boldsymbol{n}}$ is a normal vector to the interface (pointing from $j = B$ to $j = T$), and $\widehat{\boldsymbol{t}}^{(1)}$ and $\widehat{\boldsymbol{t}}^{(2)}$ are the tangent vectors. The brackets $\llbracket \cdot \rrbracket$ denote the jump condition across the interface $((j = T) - (j = B))$, and κ denotes the interfacial (mean) curvature. Note that for large-amplitude non-equilibrium situations (characterized by wave overturning and droplet entrainment), the notion of 'top' and 'bottom' fluids becomes ambiguous. However, the ambiguity is removed by identifying $j = T$ with the less viscous fluid and $j = B$ with its more viscous counterpart.

Boundary conditions are required to close the system of equations. Bounding walls with the implied no-slip boundary conditions are introduced at $z = 0$ and $z = L_z$. Inlet/outlet boundary conditions are imposed in the streamwise (x-) direction, and periodic boundary conditions in the spanwise (y-) direction: at the inlet, the velocity field is prescribed as $\boldsymbol{u}(x = 0) = (U_0(z), 0, 0)$, and at the outlet, $\partial_x \boldsymbol{u} = 0$. Here $U_0(z)$ is a prescribed *inlet condition*, the mean value of which sets the velocity scale V. Throughout this paper, the inlet condition is taken to be Poiseuille flow-profile obtained by computing the steady flat-interface solution of the Navier–Stokes equations for a particular flat-interface height h_0. At times, we also make use of periodic boundary conditions in the x-direction. Finally, the system is perturbed either through initial conditions or through a forcing localized in space; details of these are presented together with the linear and nonlinear simulation techniques in the subsequent subsections.

2.2   Linear theory

Linear theory is used in subsequent sections to study the early-time development of three-dimensional disturbances. It is shown that some of the characteristics of the linear regime are retained at later times by the subsequent nonlinear regime, thereby underscoring the importance of understanding fully the initial linear phase of the wave development. In linear theory, small-amplitude disturbances grow or decay exponentially, with growth rates and phase speeds determined from a modal Orr–Sommerfeld–Squire (OSS) eigenvalue analysis. The idea behind this approach is to linearize the equations of motion around a steady base state corresponding to uni-directional flow, to reduce the linearized equations down to an equation pair involving the wall-normal velocity and vorticity, and to Laplace–Fourier transform the resulting linear differential-algebraic equation. The transformed problem is recalled here in generic terms as follows:

$$\lambda \begin{pmatrix} \mathcal{M}_{OS} & 0 \\ \mathcal{M}_C & \mathcal{M}_S \end{pmatrix} \begin{pmatrix} \widetilde{w}_{\alpha\beta}(z,\lambda) \\ \widetilde{\omega}_{z,\alpha\beta}(z,\lambda) \end{pmatrix} = \begin{pmatrix} \mathcal{L}_{OS} & 0 \\ \mathcal{L}_C & \mathcal{L}_S \end{pmatrix} \begin{pmatrix} \widetilde{w}_{\alpha\beta}(z,\lambda) \\ \widetilde{\omega}_{z,\alpha\beta}(z,\lambda) \end{pmatrix}, \tag{2}$$

where $\mathcal{L}_{OS}$ depends on wavenumbers and the wall-normal derivative, $\mathcal{L}_{OS} = \mathcal{L}_{OS}[\mathrm{i}\alpha, \mathrm{i}\beta, \partial_z]$, and similarly for the other operators. Here, following standard notation, α denotes

a wavenumber in the streamwise direction and β denotes a wavenumber in the spanwise direction. For wall-bounded flows, solution of Equation (2) for the eigenvalue λ gives a discrete family of eigenvalues for each Fourier mode, $\{\lambda_n(\alpha, \beta)\}_{n=0}^{\infty}$. The growth rate is then determined by the eigenvalue with the largest real part. In fact, this approach is rather standard and is not discussed further here (but see Sahu & Matar (2011) and Appendix A).

2.3 Nonlinear DNS

Beyond linear theory, DNS of the Navier–Stokes equations is used in the following, through the stage of overturning waves, ligament formation and up to the point of droplet entrainment. A levelset method is utilized with a continuous surface tension model (Sussman & Fatemi, 1998). In this levelset formalism, the basic Navier–Stokes equations for density-matched fluids are modelled as

$$\left(\frac{\partial \boldsymbol{u}}{\partial t} + \boldsymbol{u} \cdot \nabla \boldsymbol{u}\right) = -\nabla p + \frac{1}{Re} \nabla \cdot \left[\mu \left(\nabla \boldsymbol{u} + \nabla \boldsymbol{u}^T\right)\right] + \delta_\epsilon(\phi)\mathcal{S}\hat{\boldsymbol{n}}\nabla \cdot \hat{\boldsymbol{n}}, \quad (3a)$$

$$\nabla \cdot \boldsymbol{u} = 0, \quad (3b)$$

$$\hat{\boldsymbol{n}} = \frac{\nabla \phi}{|\nabla \phi|}, \qquad \frac{\partial \phi}{\partial t} + \boldsymbol{u} \cdot \nabla \phi = 0. \quad (3c)$$

Here, $\phi(\boldsymbol{x}, t)$ is the levelset function indicating in which phase the point $\boldsymbol{x}$ lies ($\phi < 0$ in the bottom layer, $\phi > 0$ in the top layer). The (possibly multivalued) interface $\eta(\boldsymbol{x}, t)$ is therefore the zero level set, $\phi(\boldsymbol{x}, t) = 0 \implies \boldsymbol{x} = (x, y, \eta(x, y, t))$. Moreover, the levelset function determines the unit vector normal to the interface ($\hat{\boldsymbol{n}}$), as well as the viscosity, via the relation $\mu = m\left(1 - H_\epsilon(\phi)\right) + H_\epsilon(\phi)$. The function $H_\epsilon(\phi)$ is a regularized Heaviside function, which is smooth across a width $\epsilon = 1.5\Delta x$. Finally, $\delta_\epsilon(s) = dH_\epsilon(s)/ds$ is a regularized delta function supported on an interval $[-\epsilon, \epsilon]$. The delta function $\delta_\epsilon(s)$ is implemented either via an analytical expression for $dH_\epsilon(s)/ds$, or through finite-differencing of $H_\epsilon(\cdot)$. For the problem under consideration, both approaches yield identical results. The details of the numerical method are discussed below under several headings.

Grid structure, momentum treatment: The velocities and pressure are discretized on an isotropic MAC grid, with velocities defined at cell faces and pressures defined at cell centres, and grid spacing Δz; the timestep is denoted by Δt. The convective derivative is treated using a third-order Adams–Bashforth scheme (Boyd, 2001). The momentum fluxes are treated in a flux-conservative fashion, and the derivatives in the momentum term in the ith direction in Equation (3a) are written as follows:

$$\underbrace{\partial_x \left(\mu\partial_x u_i\right) + \partial_y \left(\mu\partial_y u_i\right) + \partial_z \left(\mu\partial_z u_i\right)}_{=\mathcal{D}_i} + \underbrace{\partial_x \left(\mu\partial_{x_i} u\right) + \partial_y \left(\mu\partial_{x_i} v\right) + \partial_z \left(\mu\partial_{x_i} w\right)}_{=\mathcal{C}_i}, \quad (4)$$

such that each derivative in the sum can be approximated numerically as a difference taken between two cell faces, thereby accurately taking account of the momentum flux between cells. The expression (4) is discretized in time using a

Crank–Nicolson treatment for the second-order manifestly diffusive terms $\mathcal{D}_i$ and a third-order Adams-Bashforth treatment for the leftover terms $\mathcal{C}_i$:

$$\tfrac{1}{2}\left(\mathcal{D}_i^{n+1} + \mathcal{D}_i^n\right) + \tfrac{23}{12}\mathcal{C}_i^n - \tfrac{4}{3}\mathcal{C}_i^{n-1} + \tfrac{5}{12}\mathcal{C}_i^{n-2}, \tag{5}$$

where n here denotes the nth timestep in the simulation. Several other methods for implementing the finite-differencing of the momentum term were attempted, but the method described here proved to be the best at capturing the stress profile across the interface.

Pressure treatment, operator inversions, levelset advection: The pressure and associated incompressibility constraint are treated using the projection method. Both the implicit momentum step and the pressure correction step call for Helmholtz's equation and Poisson's equation, respectively. For the Helmholtz step, successive over-relaxation is used. For the Poisson step, we experimented with two methods: successive over-relaxation, or GMRES with a block-Jacobi preconditioner, which was implemented using the PETSc library. The two methods yielded identical results, albeit that the code's performance was substantially improved under GMRES (Scott *et al.*, 2013*a*). Finally, the levelset function ϕ is advected using a third-order WENO scheme (Ding *et al.*, 2007), and the resulting updated levelset function is reinitialized using a Hamilton–Jacobi equation and the algorithm of Russo & Smereka (2000). The maximum curvature is limited to $1/\Delta z$.

Practical implementation: The numerical method is coded in Fortran 90 for implementation on a distributed/shared-memory architecture, using a combination of OpenMP and MPI (Gropp *et al.*, 1994). The code is run on a supercomputer in which the basic processor is an AMD Opteron 2.3GHz Interlagos processor. For a typical simulation 1024 such processors were used for 12 hours. The source code of the GMRES version is available under an open-source license (Scott *et al.* (2013*b*)).

This approach resolves large changes in interfacial topology with only a small amount of mass loss. Specifically, for a typical simulation (P4, Table 1), we computed $\max_t |V_B(t) - V_B(0)|/V_B(0) = 4\%$, where $V_B(t)$ denotes the volume of the 'bottom' phase at time t, and the maximum is taken over the full duration of the simulation. The mass loss in other simulations was similar. We have not found evidence of any parasitic currents in the simulations. These can arise in levelset methods because of the small-scale smoothing of the viscosity profile and the implementation of the continuum surface force (Meland *et al.*, 2007); their absence may be anticipated by the large streamwise velocities and rapid instability timescales that are present in the current problem. Comparisons of our results with the quasi-analytic linear theory in Section 2.2 demonstrate that the standard levelset method maintains accuracy with respect to the basic physical model in Equation (1).

The following forcing procedure was used to 'trip' the open systems investigated in this paper (i.e. those with an inlet). The z-component of Equation (3) is modified to include a localized continuous-in-time momentum forcing term $F(\boldsymbol{x}, t)$ that is compactly supported in the x-direction, and contains a polychromatic mixture of y-modes and temporal frequencies (the Fourier modes in the mixture have equal

amplitude and a random phase); specifically, we have

$$F(\boldsymbol{x}, t) = \delta_\epsilon(\phi(\boldsymbol{x}, t))\delta_{L_x}(x) \left[\frac{A_0}{N_y N_T} \sum_{i=0}^{N_y - 1} \sum_{j=1}^{N_T} \cos\left(\frac{2\pi i y}{L_y} + \frac{\Omega_C j t}{N_T} + \varphi_{ij} \right) \right], \quad (6a)$$

where

$$\delta_{L_x}(x) = \begin{cases} 1 + \cos\left[\frac{16\pi}{L_x} \left(x - \frac{1}{8} L_x \right) \right], & \frac{1}{16} L_x \le x \le \frac{3}{16} L_x, \\ 0, & \text{otherwise.} \end{cases} \quad (6b)$$

The prefactors in Equation (6a) have the effect of localizing the momentum distur-bance at the interface, and at $x = L_x/8$. (Note, the divergence of the velocity field is not disturbed by this forcing.)

The cutoff forcing frequency in Equation (6a) is taken to be $\Omega_C = 20$. For most of the parameter cases considered, this is much larger than the frequency of the linearly most-dangerous mode. However, even for those parameter cases where this condition is not satisfied, for sufficiently large amplitudes A_0, the non-passive nature (i.e. ϕ-dependence) of the forcing in Equation (6a) is important, and further frequencies are generated nonlinearly, such that the 'effective forcing' contains frequencies greater than Ω_C, including that of the linearly most-dangerous mode. Beyond the compact source region, these source-based nonlinearities play no role, except that they provide a broad spectrum of frequencies that are subsequently excited in the wave dynamics. The nonlinearities that do eventually matter for the interfacial waves are provided by the 'natural' evolution of the waves first of all in spatio-temporal linear theory and then in weakly nonlinear theory.

We shall compare and contrast results obtained with this approach not only to linear theory, but also to results of the nonlinear simulations subject to periodic boundary conditions in the x-direction (i.e., periodic conditions for velocity, whereas the periodic conditions for the pressure are such that a constant pressure drop over the unit cell is prescribed). In these periodic cases, the system is perturbed through the initial condition for the interface location; the initial conditions involve forcing spanwise modes (with a tiny contribution from streamwise modes):

$$\eta(x, y, t = 0) = h_0 + \frac{1}{9} A_0 \sum_{n=1}^{3} \sum_{m=1}^{3} \cos\left(\alpha_0 n x + \beta_0 m y + \varphi_{nm} \right)$$

$$+ \frac{1}{9} \epsilon_A \sum_{n=1}^{3} \sum_{m=1}^{3} \left[\begin{array}{c} \cos\left(n\alpha_0 x + \varphi_{nm} \right) + \cos\left(m\beta_0 y + \varphi_{nm} \right) \\ -\cos\left(2\alpha_0 n x + \beta_0 n y + \varphi_{nm} \right) - \cos\left(\alpha_0 n x + 2\beta_0 n y + \varphi_{nm} \right) \end{array} \right], \quad (7a)$$

or forcing of both streamwise and spanwise modes:

$$\eta(x, y, t = 0) = h_0 + \frac{1}{12} A_0 \sum_{n=1}^{3} \sum_{m=0}^{3} \cos\left(\alpha_0 n x + \beta_0 m y + \varphi_{nm} \right)$$

$$+ \frac{1}{12} \epsilon_A \sum_{n=1}^{3} \sum_{m=0}^{3} \left[\begin{array}{c} \cos\left(n\alpha_0 x + \varphi_{nm} \right) + \cos\left(m\beta_0 y + \varphi_{nm} \right) \\ -\cos\left(2\alpha_0 n x + \beta_0 n y + \varphi_{nm} \right) - \cos\left(\alpha_0 n x + 2\beta_0 n y + \varphi_{nm} \right) \end{array} \right] \quad (7b)$$

(note the different limits on the summation index m). Here, A_0 is some amplitude, $\varphi_{ij} \in [0, 2\pi)$ is a randomly-selected phase, and $\epsilon_A = (2.23 \times 10^{-5}) A_0$ is a small

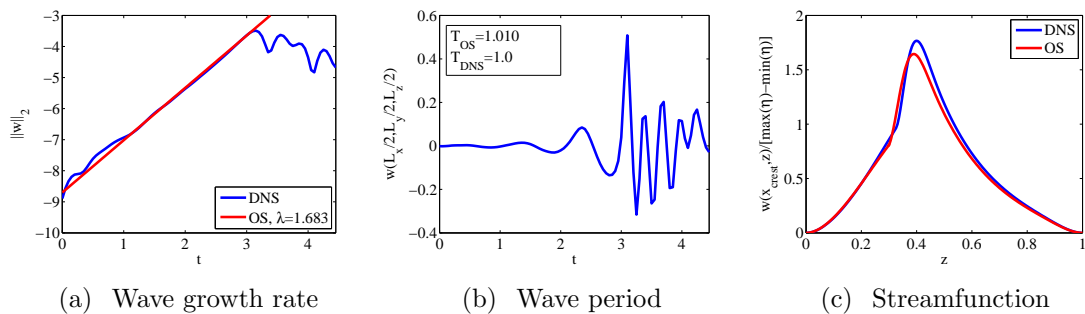(a) Wave growth rate   (b) Wave period   (c) Streamfunction

Figure 1: Validation of DNS against separate semi-analytical Orr–Sommerfeld description.

parameter. Also, $\alpha_0 = 2\pi/L_x$ and $\beta_0 = 2\pi/L_y$ are the fundamental wavenumbers in the streamwise and spanwise directions respectively. These protocols will be examined to see to what extent the three-dimensionality of the evolving waves depends on the initial conditions. Obviously, the initial conditions in Equation (7a) promote growth in the spanwise direction compared to the streamwise direction, while the initial conditions in Equation (7b) show no preference for either streamwise or spanwise waves. The development of qualitatively similar three-dimensional large-amplitude wave structures in both sets of initial conditions would be a strong indicator that such three-dimensionality is inherent in the system, rather than being a byproduct of some carefully-selected initial conditions.

Unless indication is given to the contrary, a grid spacing $\Delta z = 1/160$ is used throughout this work. This choice is checked on a case-by-case basis using the following tests: first, with $\Delta z = 1/160$, the full DNS solver reproduces the results of quasi-analytical Orr–Sommerfeld theory (e.g. Section 2.4). Also, the key nonlinear features (large-amplitude waves, wave overturning, ligaments) are virtually identical for $\Delta z = 1/160, 1/225$. Finally, the timestep is chosen such that the advective CFL number based on the maximum base-state velocity $U_0(z)$ is at most 0.2. For the small surface-tension parameters considered throughout this work, timesteps that satisfy the advective CFL criterion automatically satisfy the capillary-wave CFL condition. Note also: although not all the momentum terms are treated in a Crank–Nicolson way (see Equation (5)), for the parameters under consideration, the numerical stability of the code was not affected by the diffusive contributions in the momentum equation.

2.4 Validation of nonlinear DNS code against linear theory

The code has been rigorously validated with respect to the two-dimensional Orr–Sommerfeld quasi-analytic theory. We have computed the DNS values of the growth rate and wave speed of the most-dangerous temporal mode for the parameter values

$$(Re, r, m, \mathcal{S}) = (100, 1, 30, 0.01), \qquad h_0 = 0.3; \tag{8}$$

good agreement is obtained with respect to the eigenvalue analysis (Figure 1). The parameters Re, m, and $\mathcal{S}$ are varied throughout the work, but the density ratio is maintained at $r = 1$ and the film thickness is maintained at $h_0 = 0.3$. The
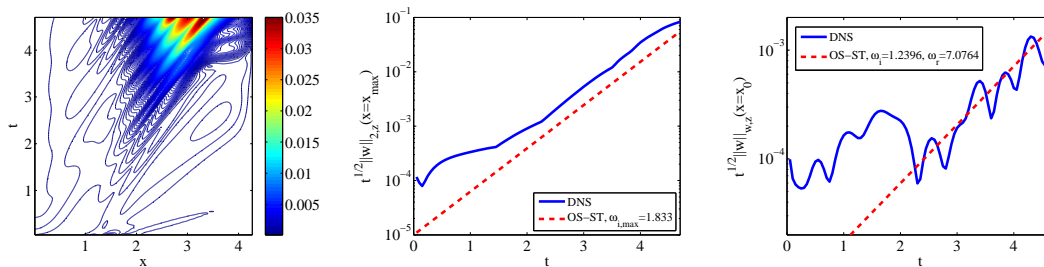
9

Figure 2: (a) Space-time plot of the norm $n(x,t)$ for the parameters in Equation (8); (b) Comparison between spatio-temporal Orr–Sommerfeld analysis and the DNS at the pulse maximum; (c) Comparison between spatio-temporal Orr–Sommerfeld analysis and the DNS at the source of the disturbance.

parameter ranges studied are motivated by the work's intended application, namely the modelling of viscous soil removal in plants during cleaning and product turnover operations (Valluri $et\ al.$, 2010). Here, $\Delta z = 1/160$ is sufficient for the simulations to have converged, with the convergence criteria as described above in Section 2.3. Also, for Equation (8), $\Delta t = 10^{-4}$ is sufficient for the advective CFL condition described in Section 2.3 to be satisfied.

As a further test, we examined the inlet/outlet version of the code, with Neumann boundary condition $\phi_x(x = 0) = \phi_x(x = L_x) = 0$, subject to an impulsive force (varying only in x; no y-dependence) applied at very early time, centred at $x = L_x/3$. We expect standard spatio-temporal Orr–Sommerfeld analysis (Ó Náraigh $et\ al.$, 2013) to apply to the present case. Thus, we predict that a two-dimensional pulse should form as a result of the imposed initial condition, whose maximum should grow at the same rate as the temporally most-dangerous mode. Moreover, the same Orr–Sommerfeld analysis demonstrates that the flow parameters (8) should produce absolute instability, in other words, disturbances grow at the location of the initial impulse, in addition to being convected downstream by the same impulse (Huerre & Monkewitz, 1990; Ó Náraigh $et\ al.$, 2013). It is therefore also expected that the disturbance should grow at the source, with a growth rate given by the value of the Orr–Sommerfeld frequency $\Omega(\alpha)$ evaluated at the saddle point in the complex α-plane. A spacetime plot of the pulse norm

$$n(x,t) = \left(\int_0^1 |w(x,z,t)|^2 \mathrm{d}z \right)^{1/2}$$

is therefore shown in Figure 2(a) (w represents the perturbation velocity in the wall-normal direction, see Appendix A). Information from this plot is extracted in Figure 2(b), where the pulse maximum is followed. The pulse maximum grows at the same rate as the temporally most-dangerous mode as computed by the Orr–Sommerfeld analysis. Furthermore, the instability grows at the source (absolute instability), and the numerical growth rate is in agreement with the theoretical growth rate computed from the saddle-point of the complex Orr–Sommerfeld eigenvalue analysis. The measured period in Figure 2(c) is 0.9 ± 0.1. The apparent period is only half this amount, because absolute values are taken in plotting $n(x,t)$, rather than a signed velocity. The theoretical value of the period is $2\pi/7.095 = 0.8856$.
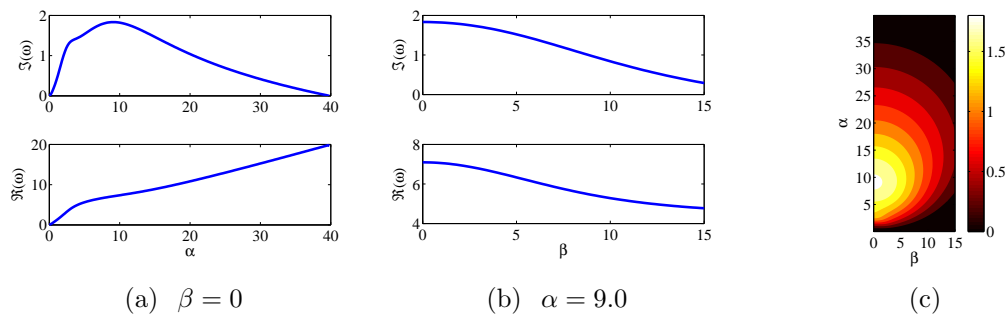
10

Figure 3: Modal growth rates obtained directly from solving the Orr–Sommerfeld–Squire problem. Here, $(m, Re, \mathcal{S}) = (30, 100, 0.01)$.

Thus, the numerical period and the theoretical periods (equivalently wave speeds) agree. The growth rates are also in agreement. A final test involves the study of a parameter class that is convectively unstable. Specifically, we repeated these DNS calculations with $Re = 40$ (the other parameters in Equation (8) remaining the same). Standard spatio-temporal Orr–Sommerfeld analysis indicates that this parameter class is convectively unstable. This is confirmed by the DNS (not shown): the norm $n(x, t)$ decays at the source location, while the growing disturbance is convected downstream; and grows at a rate corresponding to the temporally most-dangerous mode computed from Orr–Sommerfeld analysis. Further tests concerning the full Orr–Sommerfeld–Squire analysis (not shown here, but demonstrated throughout the paper) demonstrate that numerical method also captures the three-dimensional modes.

3   Modal linear growth

We use the approach based on linear theory outlined in Section 2.2 to study the initial growth of small-amplitude waves, outlining several features of the dispersion relation for future reference. The calculations are carried out for the parameter values $m = 30$, with various values of $\mathcal{S}$ and Re. Figure 3 shows the Orr–Sommerfeld–Squire growth rates for the parameter set $(m, Re, \mathcal{S}) = (30, 100, 0.01)$. A large range of modes is unstable. The most-dangerous modes are streamwise, and the α-dispersion relation in Figure 3(b) is 'flat', such that a band of unstable wavenumbers with very similar growth rates is excited. Upon increasing the surface tension but leaving the other parameters the same, similar features pertain (Figure 4). Here, however, the spanwise growth rates are much smaller than the streamwise ones, and the range of excited modes is narrower. Note also that the α-dispersion relation is flatter than before. Consideration is also given to a situation wherein a very narrow range of modes is excited $((m, Re, \mathcal{S}) = (30, 300, 0.3)$, Figure 5). The dispersion relation (Figure 5(b)) now possesses a sharp peak at $\alpha \approx 4.2$, such that a single mode will feature prominently in the evolution of the interface. Also, in spite of the larger Reynolds number than before, three-dimensional waves are more stable in this situation, and only a narrow range of spanwise waves are unstable. These dispersion relations will be used subsequently to explain the linear and weakly nonlinear
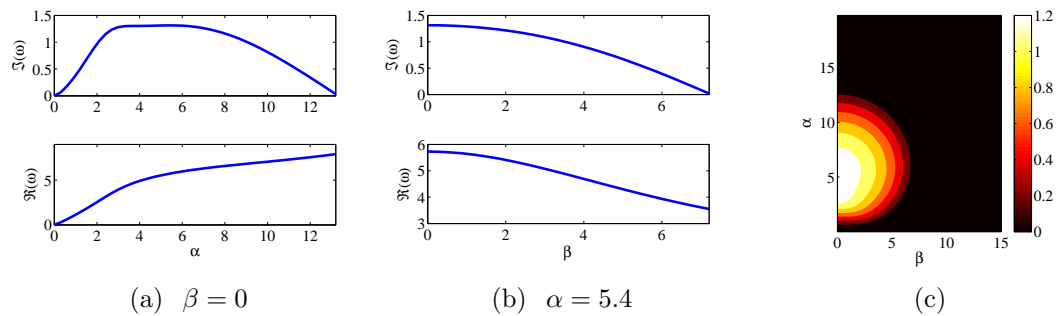
11

(a) $\beta = 0$ (b) $\alpha = 5.4$ (c)

Figure 4: The same as Figure 3, but with $(m, Re, \mathcal{S}) = (30, 100, 0.1)$.

(a) $\beta = 0$ (b) $\alpha = 4.2$ (c)
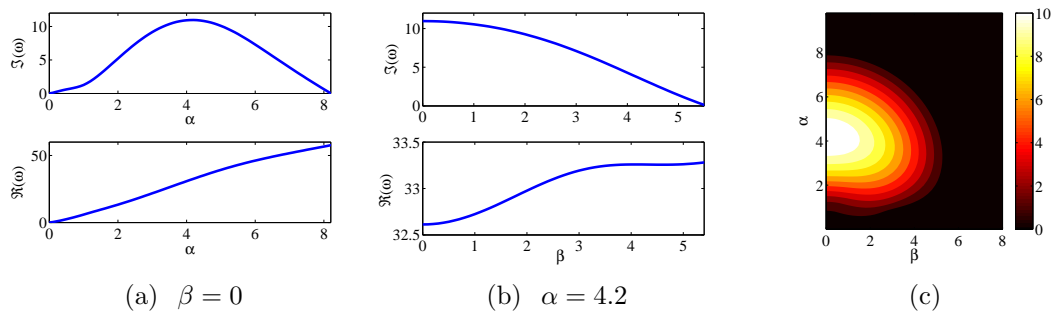
Figure 5: The same as Figure 3, but with $(m, Re, \mathcal{S}) = (30, 300, 0.3)$.

evolution of the interfacial waves in the full DNS.

## 4   Linear and nonlinear waves in periodic simulations

We begin the presentation of results obtained with direct numerical simulations of cases wherein streamwise-periodic boundary conditions are used. Although these boundary conditions do not reflect the behaviour of a real system, it is appropriate to consider such simulations, for a number of compelling reasons: first, these simulations comprise a 'clean' database, wherein only a small number of modes is active initially, and wherein issues surrounding spatio-temporal growth do not enter, such that the growth of waves can be investigated unambiguously in the framework of linear theory. Also, although a Fourier transform may be taken in a non-periodic domain, the results there are ambiguous because of boundary effects, and such a decomposition is more appropriate in a periodic system. A brief summary of the most important simulations performed is given in Table 1; further detail is presented below in the text.

4.1   Subcritical route to three-dimensional waves

Consideration is first given to the simulation P3, involving the parameter set $(m, Re, \mathcal{S}) = (30, 300, 0.3)$. The Orr–Sommerfeld–Squire analysis in Section 3 indicates that this parameter set produces instability, with large temporal growth rates for streamwise waves, and no temporal growth for waves with spanwise components. The same

12

Case	Parameters	Geometric Parameters	Figure
P1	$A_0 = 0.002$, $\mathcal{S} = 0.01$, $Re = 100$, ICs: Equation (7a)	$(L_x, L_y, L_z) = (2, 1, 1)$	Figure 7
P2	$A_0 = 0.002$, $\mathcal{S} = 0.01$, $Re = 100$, ICs: Equation (7b)	$(L_x, L_y, L_z) = (2, 1, 1)$	Figure 8
P3	$A_0 = 0.02$, $\mathcal{S} = 0.3$, $Re = 300$, ICs: Equation (7a)	$(L_x, L_y, L_z) = (1.58, 1, 1)$	
P4	$A_0 = 0.02$, $\mathcal{S} = 0.1$, $Re = 100$, ICs: Equation (7a)	$(L_x, L_y, L_z) = (2, 1, 1)$	

Table 1: Summary of the main periodic simulations, with $m = 30$.

(a) (b)
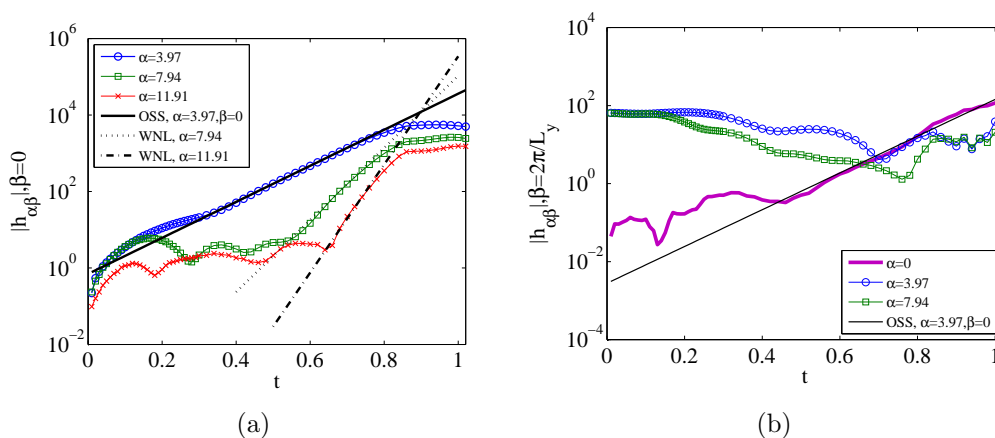
Figure 6: Interfacial spectra for the case P3. (a) Streamwise modes. (b) Spanwise modes, with $\beta = 2\pi/L_y$. Both figures show the action of weakly nonlinear mechanisms. In particular in (b) the growth of the purely spanwise mode with $\alpha = 0$ is shown.

quasi-analytical theory predicts that for the geometry prescribed in the P3 simulation, only one unstable mode should be present, with $\alpha = 3.97$ and $\Omega_i = 10.85$.

The inception of the three-dimensional wave structures in the DNS takes place at early times, when the wave amplitudes are small. To understand this genesis, spectra of the interface height were taken at different times. The spectrum is computed with respect to the interface $\eta(x, y, t)$, defined as follows:

$$\eta(x, y, t) = \min_i Z(x, y, t), \qquad Z(x, y, t) = \{z_i | \phi(x, y, z_i, t) = 0, i = 1, 2, \cdots\}. \quad (9)$$

For small-amplitude waves, $i = 1$ only, corresponding to a situation wherein there are no overturning waves, droplets, or ligaments. For $i > 1$, the interfacial spectrum loses any definite meaning, and spectral data in this regime are not discussed further. The results of the spectral analysis are shown in Figure 6. Figure 6(a) shows a time series of the streamwise modes only. The mode $\alpha = 3.96$ grows exponentially fast, at a rate given by OSS theory. As further predicted by the same theory, the other modes do not grow initially. However, as time goes by, the other modes undergo

exponential growth, in a manner that is perfectly consistent with weakly nonlinear theory (Barthelet *et al.*, 1995): the nth multiple of the fundamental wavenumber $\alpha = \alpha_0 = 3.97$ grows at a rate $n\Omega_{\text{i}}(\alpha_0)$. This agreement is particularly appropriate, as the parameters in the case P3 are such that only one mode is initially linearly unstable, such that other modes (overtones) become 'enslaved' to the single dominant mode and grow exponentially at integer multiples of the growth rate of the fundamental.

Consideration is also given to spanwise modes with $\beta = \beta_0 := 2\pi/L_y$ (Figure 6(b)), wherein an interesting feature arises: the purely spanwise mode $(\alpha = 0, \beta_0)$ that is stable in normal-mode linear theory grows exponentially at the same rate as the streamwise most-dangerous mode $(\alpha = 3.96, \beta = 0)$. It is as if the purely spanwise mode is slaved to the most-dangerous streamwise mode. Further streamwise modes at $(\alpha \neq 0, \beta_0)$ are also excited nonlinearly, but their amplitude remains small compared to the exponentially-growing mode until close to the wave turnover time. Thus, in a first approximation, the purely spanwise mode (i.e. $(\alpha \neq 0, \beta_0)$) can be viewed as behaving nonlinearly, while all other relevant modes behave according to linear theory. This additional enslavement of the purely spanwise mode is explained in generic terms without resort to a full resolution of the amplitude equations in a weakly nonlinear analysis. The interface is decomposed into its constituent Fourier modes:

$$\eta(\boldsymbol{x}_\perp, t) = \sum_{\boldsymbol{p}} A_{\boldsymbol{p}}(t) e^{i\boldsymbol{p}\cdot\boldsymbol{x}_\perp}, \qquad \boldsymbol{x}_\perp = (x, y),$$

$$\boldsymbol{p} := (\alpha, \beta) = \left(\frac{2\pi p_x}{L_x}, \frac{2\pi p_y}{L_y}\right), \qquad p_x, p_y \in \mathbb{Z}. \quad (10a)$$

Generically, the equations for the amplitudes $A_{\boldsymbol{p}}$ can be written as follows:

$$\frac{dA_{\boldsymbol{p}}}{dt} = \lambda_{\boldsymbol{p}} A_{\boldsymbol{p}} + \sum_{\boldsymbol{q}} \mathcal{M}(\boldsymbol{q}, \boldsymbol{p}) A_{\boldsymbol{q}} A_{\boldsymbol{p}-\boldsymbol{q}} + \sum_{\boldsymbol{q}} \sum_{\boldsymbol{r}} \mathcal{N}(\boldsymbol{q}, \boldsymbol{r}, \boldsymbol{p}) A_{\boldsymbol{q}} A_{\boldsymbol{r}} A_{\boldsymbol{p}-\boldsymbol{q}-\boldsymbol{r}}, \quad (10b)$$

where we have truncated the expression at cubic order in the amplitudes. We focus on the mode $\boldsymbol{p} = (0, \beta_0)$. We examine mode combinations $(\boldsymbol{p}, \boldsymbol{p} - \boldsymbol{q})$ and $(\boldsymbol{q}, \boldsymbol{r}, \boldsymbol{p} - \boldsymbol{q} - \boldsymbol{r})$ corresponding to amplitudes that do not decay rapidly in linear theory. For this reason, wavenumbers with $|\beta| = 2\beta_0$ and higher are neglected on the right-hand side of Equation (10b), since it is known from linear theory and from spectral analysis of the full DNS that the full (α, β) spectrum decays rapidly as $|\beta|$ moves away from zero. Under these restrictions, only quadratic contributions play a role for the case $\boldsymbol{p} = (0, \beta_0)$. Also, only the modes $\boldsymbol{q} = (\pm\alpha_0, 0)$ and $\boldsymbol{q} = (\pm\alpha_0, \beta_0)$ enter into the interaction term (here $\alpha_0 := 2\pi/L_x$). This results in the following reduced amplitude equation:

$$\frac{dA_{\boldsymbol{p}}}{dt} = \lambda_{\boldsymbol{p}} A_{\boldsymbol{p}} + \mathcal{M}[\boldsymbol{p}, (\alpha_0, 0)] A_{(\alpha_0,0)} A_{(-\alpha_0,\beta_0)} + \mathcal{M}[\boldsymbol{p}, (\alpha_0, \beta_0)] A_{(-\alpha_0,0)} A_{(\alpha_0,\beta_0)}$$

$$+ \mathcal{M}[\boldsymbol{p}, (-\alpha_0, \beta_0)] A_{(\alpha_0,0)} A_{(-\alpha_0,\beta_0)} + \mathcal{M}[\boldsymbol{p}, (-\alpha_0, 0)] A_{(-\alpha_0,0)} A_{(\alpha_0,\beta_0)}. \quad (10c)$$

Typically, Equation (10c) is supplemented with a set of equations for other relevant amplitudes which together form a finite set of interacting modes, leading to a closed

system of nonlinear amplitude equations (Schmid & Henningson, 2001). However, here the argument is continued in a more heuristic way as follows. Given the evidence in Figure 6(a)–(b), in a first approximation, over the time interval of interest, where the amplitude A_{0,β_0} grows significantly, the modes $(\pm\alpha_0, 0)$ can be treated as growing according to linear theory, while the modes $(\pm\alpha_0, \beta_0)$ can be treated as merely oscillatory, having no growth. Also, $\overline{A_{\alpha_0,0}} = A_{-\alpha_0,0}$, since $\eta(\boldsymbol{x}_\perp, t)$ is real. Equation (10c) can be simplified further by 'bundling up' the oscillatory functions as follows:

$$\frac{dA_{\boldsymbol{p}}}{dt} = \lambda_{\boldsymbol{p}} A_{\boldsymbol{p}} + C(t) e^{\Omega_{\mathrm{i}}(\alpha_0, 0)t} \tag{10d}$$

where $C(t)$ is a bounded linear combination of sinusoidal oscillatory functions. Equation (10d) is a standard linear first-order ODE, whose asymptotic solution is $A_{\boldsymbol{p}} \propto e^{\Omega_{\mathrm{i}}(\alpha_0, 0)t}$, in other words, the purely spanwise mode $\boldsymbol{p} = (0, \beta_0)$ is slaved to the most-dangerous streamwise mode.

4.2 Supercritical route to three-dimensional waves – linear regime

We also consider parameter sets far from criticality. We start by examining the parameters in Equation (8), recalled here as $(Re, m, \mathcal{S}) = (100, 30, 0.01)$. For these parameters, under linear theory, two-dimensional and three-dimensional waves are strongly amplified, with growth rates that are comparable in magnitude (e.g. Figure 3); in particular,

$$\frac{\Omega_{\mathrm{i}}(\alpha = 9.42, \beta = 0)}{\Omega_{\mathrm{i}}(\alpha = 9.42, \beta = 2\pi/L_y)} = \frac{1.832}{1.364} \approx 1.343,$$

from the same Orr–Sommerfeld–Squire analysis. Before examining the interfacial spectra in detail, some qualitative observations are made about the interfacial evolution in general. Snapshots of the interface configuration for cases using Equation (7a) (P1) and (7b) (P2) as periodic initial conditions are presented in Figures 7 and 8, respectively. Recall that the different initial conditions are given by Equation (7).

After an initial regime of wave growth, wave overturning takes place, and large three-dimensional structures form. By comparing Figures 7 and 8, it is clear that the same nonlinear features appear in both simulations, regardless of the relative strength of the streamwise compared to the spanwise modes in the initial condition, albeit that for the case P1, the nonlinear waves possess less symmetry in the spanwise direction. This confirms the hypothesis that three-dimensional structures are intrinsic to the system, and are not a mere byproduct of a contrived selection of the initial data.

We have investigated briefly the physical mechanism that governs early-stage small-amplitude wave growth. By analysing the tangential-stress distribution at the interface, we have confirmed that the results from the DNS support the standard conclusion from linear theory that the instability is precipitated by a mismatch in the viscosity across the interface (e.g. Yih (1967); Boomkamp & Miesen (1996)).

Figure 9 shows time series of interfacial spectra. It is clear from this figure that the streamwise and spanwise waves that develop on the interface in the snapshots

(a) $t = 1.0$ (b) $t = 2.0$ (c) $t = 3.0$

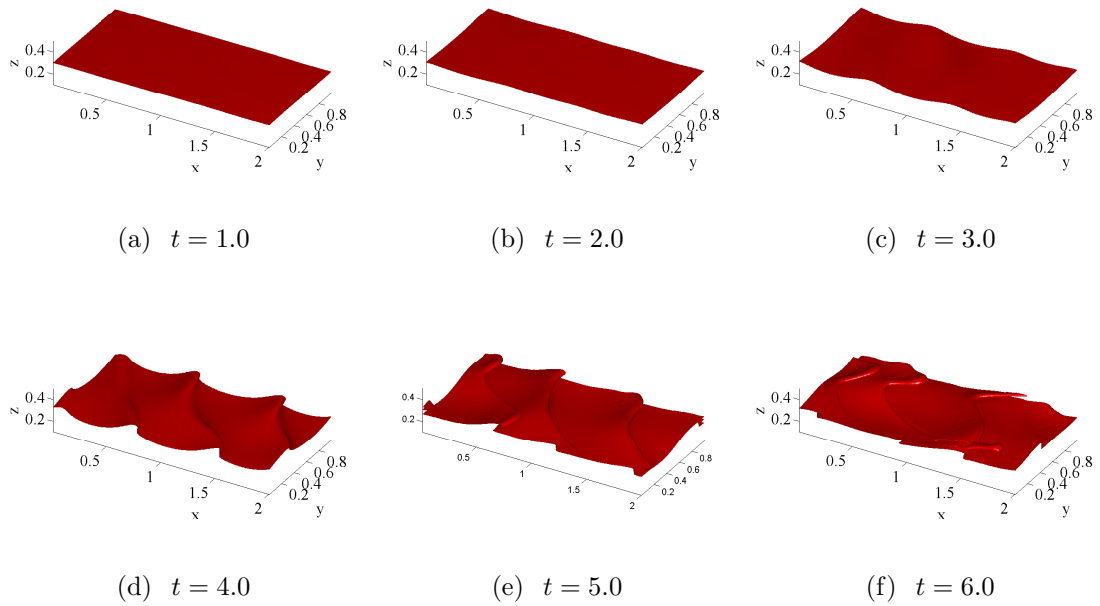(d) $t = 4.0$ (e) $t = 5.0$ (f) $t = 6.0$

Figure 7: DNS solution for case P1 ($\mathcal{S} = 0.01$, $A_0 = 0.002$, and initial conditions given by Equation (7a)). Snapshots of the interface profile at various times, coloured by wave elevation from black ($z = 0.25$) to white ($z = 0.4$).
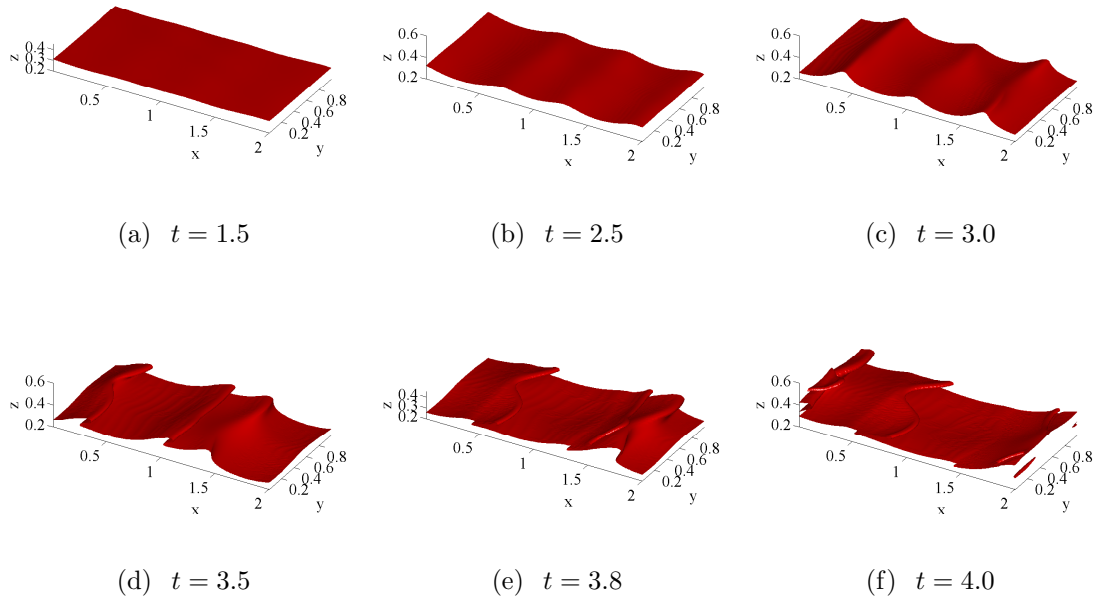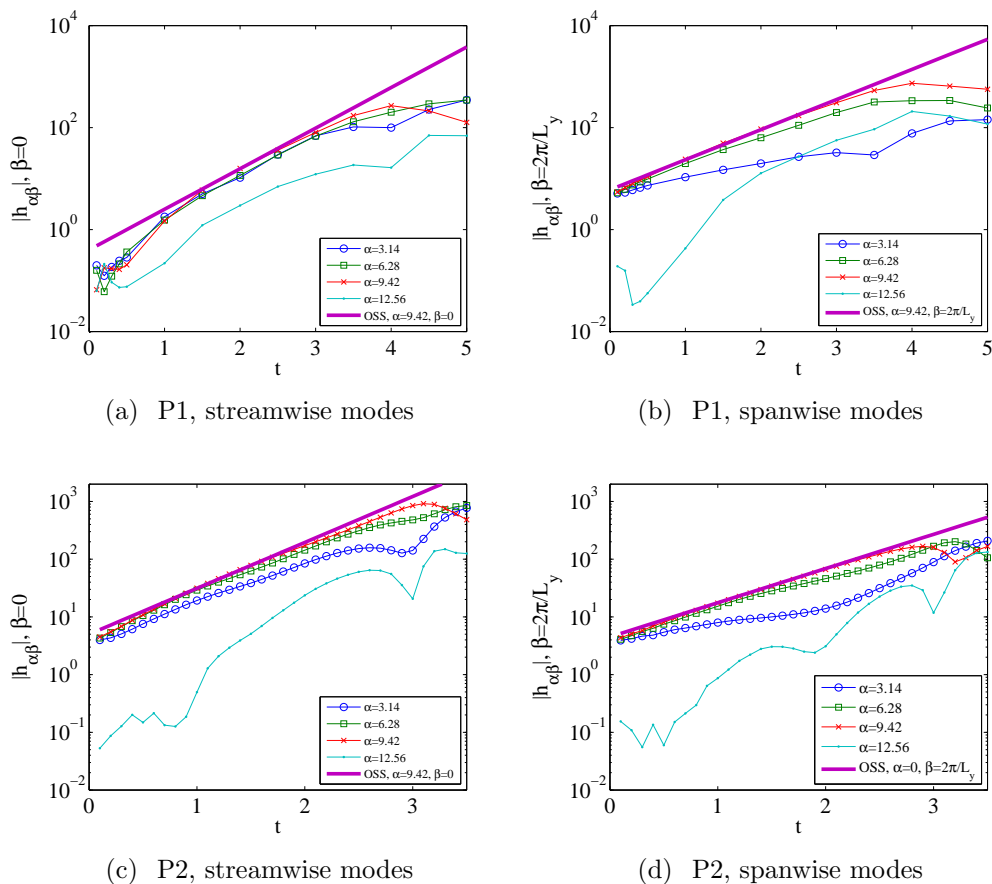

(a) $t = 1.5$ (b) $t = 2.5$ (c) $t = 3.0$

(d) $t = 3.5$ (e) $t = 3.8$ (f) $t = 4.0$

Figure 8: DNS solution for case P2 ($\mathcal{S} = 0.01$, $A_0 = 0.002$, and initial conditions given by Equation (7b)). Snapshots of the interface profile at various times, coloured by wave elevation from black ($z = 0.25$) to white ($z = 0.55$).

(a) P1, streamwise modes

(b) P1, spanwise modes

(c) P2, streamwise modes

(d) P2, spanwise modes

Figure 9: Interfacial spectra for the cases P1 and P2. (a), (b) P1, with spanwise-dominant forcing; (c), (d) P2, with an equal mixture of spanwise and streamwise modes. Here $(Re, m, \mathcal{S}) = (100, 30, 0.01)$, and $A_0 = 0.002$. The downwards-pointing kinks coincide with wave overturning.

in Figures 7–8 arise directly from linear theory: the streamwise and spanwise 'long' waves with $\alpha = 3.14, 6.28, 9.42$ in Figure 9 enjoy a period of exponential growth at a rate given by Orr–Sommerfeld–Squire theory (shorter waves exhibit weak nonlinearity and are discussed briefly below Section 4.3). A further comparison between the interfacial snapshots and the spectral plots in Figure 9 indicates that the interfacial waves grow according to linear theory until close to the point of overturning. This is similar to the behaviour observed in prior studies for related two-dimensional flows (Valluri *et al.*, 2007, 2010). From the interfacial snapshots, the overturning time is $t = 4.0$ in Figure 7 and $t = 3.0$ in Figure 8. (The overturning is retarded in Figure 7 because of the suppression of the most-dangerous spanwise modes in the initial conditions in Equation (7a) compared to Equation (7b)). Also, in Figure 9, 'kinks' in the time series of the spectral amplitudes signal wave overturning, and roughly coincide with the end of the regime of exponential growth in the amplitudes (i.e. the end of the regime of linearized dynamics).

The fact that linear theory applies to the DNS in Figure 9 even at late times, up to the onset of wave overturning, can be used to explain further the origin of and lead-up to the wave coalescence in Figures 7 and 8. In particular, three wave
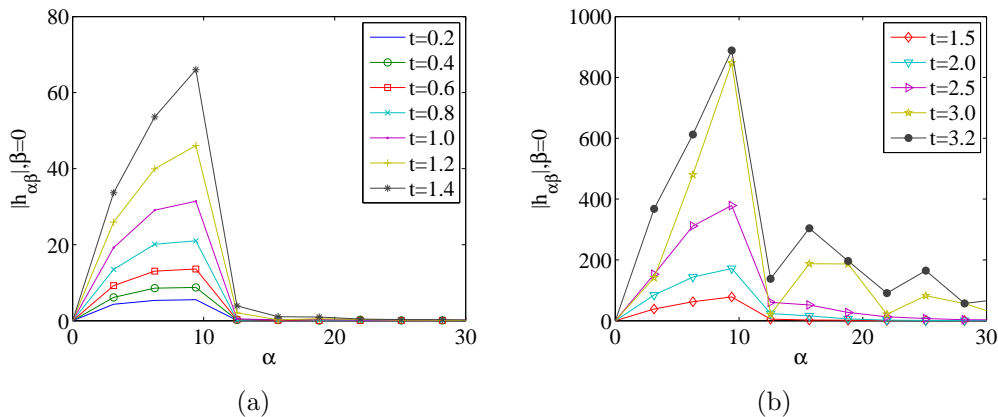
Figure 10: Snapshots of the interfacial spectra (streamwise modes) for the case P2. (a) Linear regime; (b) weakly non-linear regime.

crests are visible in Figure 8 at $t = 3.0$. The distance between the two leftmost wave crests decreases over time; by the time overturning takes place at $t = 3.8$, the two wave crests are coincident, and this leads to a complicated nonlinear interaction whereby the topmost overturned wave undergoes elongation and ligament formation. The lead-up to this coalescence-type event is readily explained by linear theory: in Figures 3–4, the dispersion curve for the two cases $\mathcal{S} = 0.01, 0.1$ are extremely flat, such that the amplification of the most-dangerous mode is comparable in magnitude to that of neighbouring modes in Fourier space. Thus, a band of waves is selected by the instability, each of which has a distinct phase velocity, thereby creating a situation wherein the waves 'race' each other. Clearly, in a linear regime, such racing waves will merely pass through one another. However, in Figure 8 the merging of the waves under the linear 'racing' phenomenon coincides with wave overturning, such that the two overturned waves become 'locked in' to one another, leading to the complicated structures seen in Figure 8(e)–(f).

4.3 Supercritical route to three-dimensional waves – nonlinear regime

Consideration is also given to snapshots of the interface spectra, at various times, focusing on streamwise modes (Figure 10). Our purpose here is to investigate the weakly nonlinear regime of the wave evolution - no matter how brief this may be. For, although Figure 10(a) and earlier figures (e.g. Figures 7–9) demonstrate that the results of linear theory pertain for long waves up until near the point of wave overturning, such overturning necessarily has its origin in the presence of the nonlinear terms in the full Navier–Stokes equations. Also, it is of inters to understand the discrepancy in Figure 9, wherein the relatively short wave at $\alpha = 12.56$ grows at a faster rate than that predicted by linear theory. Thus, in Figure 10, snapshots of the streamwise modal spectra at relatively late times (i.e. just prior to overturning) are examined. The most salient finding is that the simplified weakly non-linear theory in the work by Barthelet *et al.* (1995) do not pertain: not only overtones of the linearly most-dangerous mode, but also other combinations are present. This is eas-

18

ily explained however by the fact that the parameter regime under investigation is far beyond criticality. Indeed, the most prominent wave to be excited in the weakly non-linear regime is at $\alpha = 15.70$, which suggests a three-wave interaction involving the linearly-excited modes at $\alpha = 6.28$ and $\alpha = 9.42$. The second most-prominent wave to be excited in the non-linear regime is indeed an overtone of the linearly most-dangerous mode at $\alpha = 9.42$, which contributes to the steepening of said wave in real space.

Thus, the relatively short waves in the simulation are amplified at rates above those implied by linear theory. This fact can also be used to explain why the relatively short wave at $\alpha = 12.56$ does not obey linear theory, whereas longer waves ($\alpha = 3.14, 6.28, 9.42$) do. Finally, in real space, the nonlinear wave combinations do not saturate, but rather overturn, and a combination of spanwise growing waves with an overturning streamwise wave produces the ligaments seen in Figure 8. From these findings for a system far from criticality, it is concluded that linear theory plays a large role in determining the final three-dimensional wave structures that appear in the system. In particular, it is demonstrated that three-dimensional waves that initially grow exponentially are further amplified at late times, and develop finally into nonlinear three-dimensional ligaments. The mechanism for the creation of this final state is described in detail in a later section (Section 6), where we demonstrate that its origin is kinematic rather than dynamic, and arises because the persistent spanwise waves undergo distortion and stretching under the action of the mean flow.

Consideration is also given to the robustness of the weakly nonlinear theory for spanwise modes developed in Section 4.1 (e.g. Equations (10)). Although the discussion in Equations (10) takes place in the context of a simulation wherein only a single streamwise mode is linearly unstable, the derivation of Equation (10d) will carry over in an approximate sense to the cases P1,P2, and P4, due to the following chain of arguments. For, only a number of unstable modes fit inside the periodic channels. In the simulations P1–P2 and P4, the dispersion relations are 'flat', meaning that all unstable modes have a growth rate comparable to the most-dangerous modal growth rate. The spanwise (linearly stable) mode will therefore 'see' the streamwise modes as a single unstable mode, and under the coupling described in Equation (10), will be amplified at (close to) the maximal rate. By examining relevant spectra (Figure 11(a)), we have confirmed that this is indeed the case: in the simulations P1–P2 considered earlier, after some transience, the purely spanwise mode $(0, 2\pi/L_y)$ does indeed grow at the same rate as the most-dangerous (streamwise) mode. However, given the long transient time before such weakly nonlinear interactions enter, the simulation is utterly dominated by the modes that are linearly unstable. This reflects the strong supercriticality of this parameter set. A further simulation (P4) is intermediate between (P1,P2) and P3: both the direct mechanism and the weakly nonlinear mechanism play a role in producing the three-dimensional waves (Figure 11(b,c)).

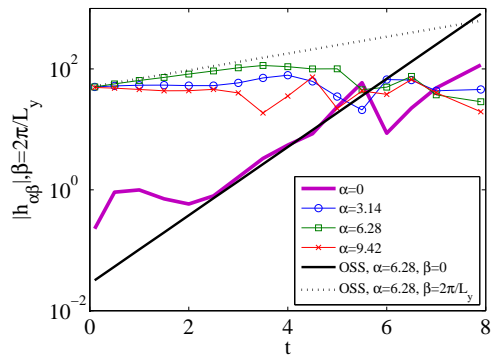## 5 Linear and nonlinear waves in open flows

We perform fully nonlinear simulations for long open channels, with L_x between 3.16 and 8.0. The aim is to investigate whether the findings obtained for wave growth in
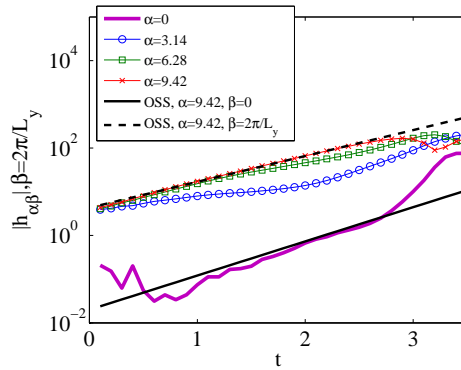
(a) P1 revisited, spanwise
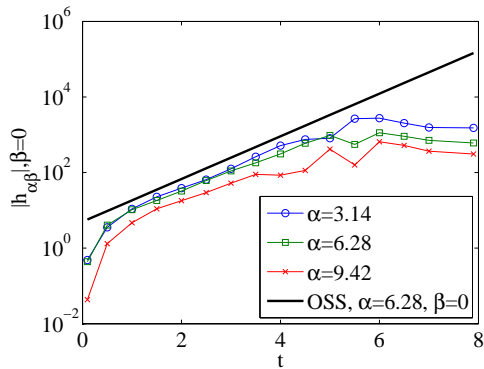
(b) P4, streamwise

(c) P4, spanwise

Figure 11: Interfacial spectra for the cases P1, P4. (a) Case P1 revisited, streamwise modes. (b) Streamwise modes, P4 (c) Spanwise modes, P4, with $\beta = 2\pi/L_y$.
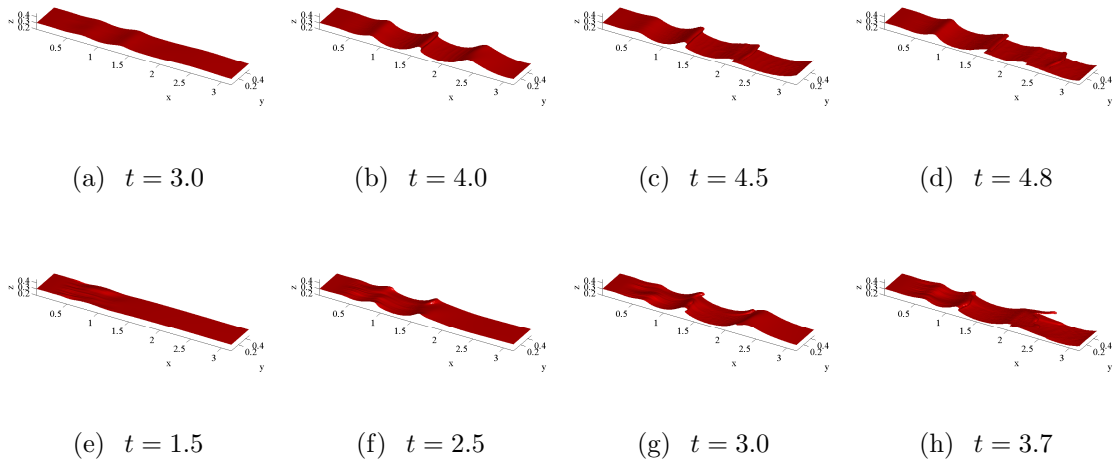
(a) $t = 3.0$ (b) $t = 4.0$ (c) $t = 4.5$ (d) $t = 4.8$

(e) $t = 1.5$ (f) $t = 2.5$ (g) $t = 3.0$ (h) $t = 3.7$

Figure 12: Effect of forcing amplitude on nonlinear channel flow DNS: top row, case CH1 ($A_0 = 10$); lower row, CH4 ($A_0 = 100$). Snapshots of the interface profile at various times.

periodic domains carry over to open flows. In contrast to periodic cases, the forcing is localized in space, but continuous in time (Equation (6)). The simulations are summarized in Table 2 and 3 and are reported below in the text in more detail.

A parametric study of the effect of the forcing amplitude A_0 on the interface evolution is conducted, the results of which are summarized in Table 2 (CH1–CH4). Further simulations on a wider domain are also considered (CH5 , Table 3). The simulations have been carried out over a long period of time $t_{\max} = 5$. Snapshots of the interface shape for CH1 ($A_0 = 10$) are shown in Figure 12 (upper row), which are compared with CH4 ($A_0 = 100$) in the lower row. The case CH4 can be compared directly with Figure 13, where a wider domain was used with the same forcing parameters; in the latter, a somewhat more three-dimensional flow is observed, but the main flow behaviour is similar. From the results shown in Figure 12 it is concluded that the strength of the forcing has only a limited effect on the subsequent ligament formation: the remaining trend is that the transverse disturbances are more pronounced when the forcing amplitude is larger. Furthermore, comparison with results for the periodic system in Figures 7-8 shows these to be qualitatively similar, indicating that the physical mechanisms that drive the development towards ligament formation persist under changes in the forcing mechanisms. Finally, the main strong nonlinear flow behaviour in the CH5 simulation is illustrated in Figure 13(e), where the interface exhibits 'sheet'-like ligaments downstream at a late stage. This behaviour is examined further with respect to other simulations, corresponding to different values of Re and $\mathcal{S}$.

A simulation with stronger surface tension has also been conducted (CH6, Table 3). Snapshots of the interface at various times are presented in Figure 14. In contrast to the simulations CH1-CH5 where the overturned waves formed 'sheets', the late-time evolution of CH6 exhibits a highly-elongated ligament, attached to an otherwise more-or-less two-dimensional structure. However, the contrasts between CH5 and CH6 are largely superficial: not only do the three-dimensional waves and

21

Case	Parameters	Description	Figure
CH1	$A_0 = 10$	Wave formation at the forcing location. The initial waves are strongly two-dimensional. As the disturbances propagate downstream, three-dimensional waves form (wavelength $2\pi/L_y$).	Figure 12 (a)-(d)
CH2	$A_0 = 20$	The same as CH1	
CH3	$A_0 = 50$	The same as CH1	
CH4	$A_0 = 100$	Similar to CH1: Wave formation at the forcing location. The initial waves are largely two-dimensional, with small components in the spanwise direction. The waves grow and become more two dimensional as they are carried downstream. However, the three-dimensionality is not quenched: in fact, at late times, it is enhanced as in the CH1 case, thereby leading to a variety of structures with spanwise wavelengths L_y and shorter.	Figure 12 (e)-(h)

Table 2: Parametric study showing the effects of varying the forcing amplitude. Fluid parameters: $(Re, m, \mathcal{S}) = (100, 30, 0.01)$. Geometric parameters: Simulations CH1-4 $(L_x, L_y, L_z) = (3.16, 0.5, 1)$.

Case	Parameters	Description	Figure
CH5	$A_0 = 100$, $\mathcal{S} = 0.01$	Similar to CH5, but with $(L_x, L_y, L_z) = (3.16, 1, 1)$ and a correspondingly more three-dimensional flow.	Figure 13
CH6	$A_0 = 300$, $\mathcal{S} = 0.1$	Long channel, with $(L_x, L_y, L_z) = (8.0, 1, 1)$. Strongly two-dimensional wave evolution, with three-dimensional disturbances developing along wave crests. The disturbances form into elongated ligament structures ('fingers').	Figure 14

Table 3: Parametric study showing the effects of varying the surface tension. Other parameters: $(Re, m) = (100, 30)$.
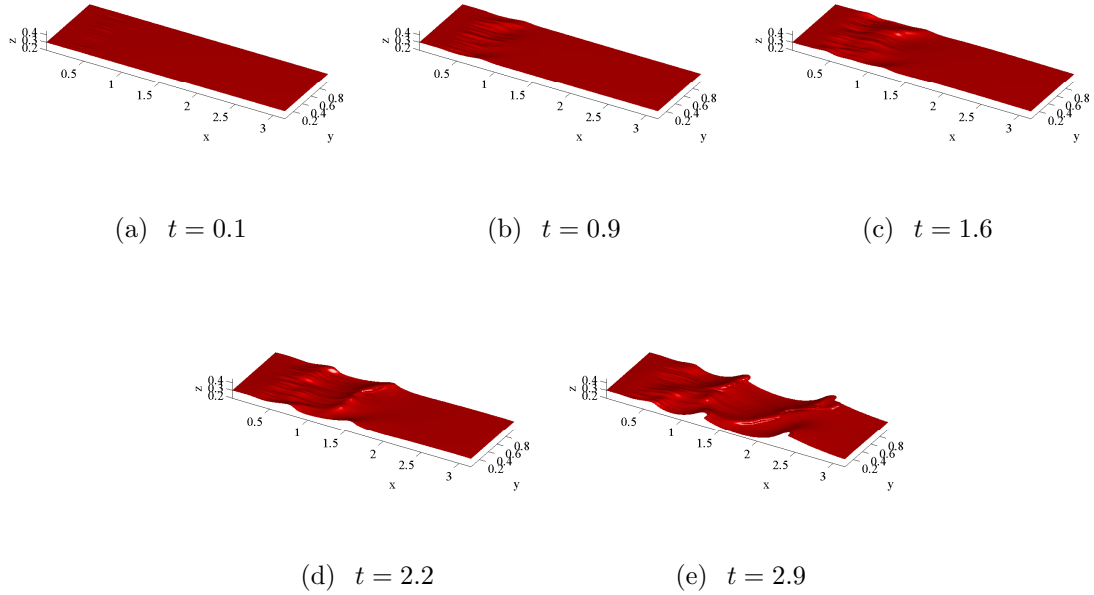
(a) $t = 0.1$

(b) $t = 0.9$

(c) $t = 1.6$

(d) $t = 2.2$

(e) $t = 2.9$

Figure 13: DNS for high-surface-tension case CH5 – snapshots of interfacial configuration at various times.

(a) $t = 1.5$

(b) $t = 2.5$

(c) $t = 3$

(d) $t = 3.5$

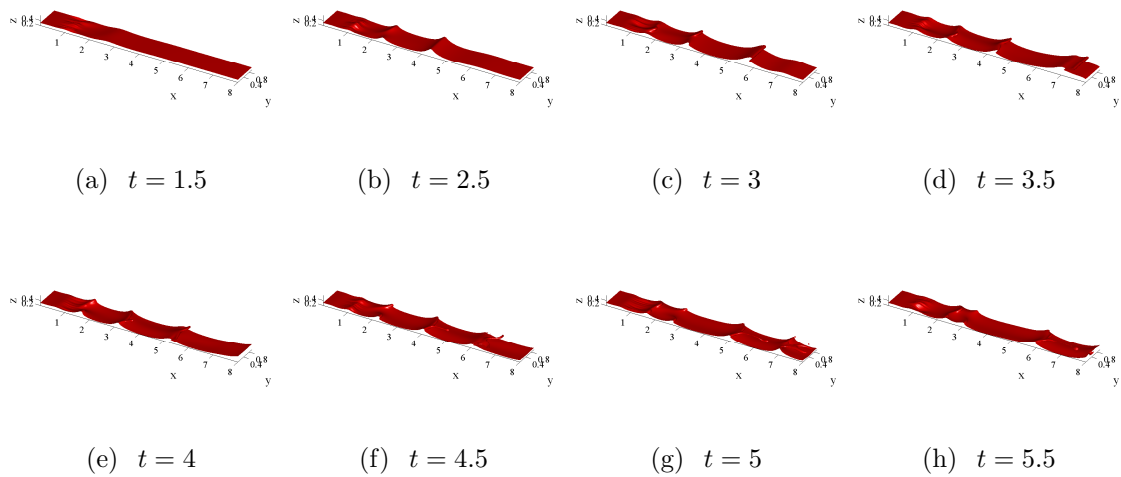(e) $t = 4$

(f) $t = 4.5$

(g) $t = 5$

(h) $t = 5.5$

Figure 14: DNS for high-surface-tension case CH6 – snapshots of interfacial configuration at various times.

subsequent sheet/ligament formation owe their origin to the same linear and weakly nonlinear theories but in addition, careful consideration of further distinct parameter values (specifically, CH7, see Section 6) demonstrates that the two distinct phenomena can co-exist. Finally, for open flows, comparisons with linear theory are best presented not through spectra, but rather through an examination of the spacetime evolution of the maximum interfacial curvature (for similar ideas in two dimensions, see the work by Valluri *et al.* (2010)). This is done in the next section.

6   Ligament formation and dynamics/kinematics

Having characterized the three-dimensional waves in the linear and weakly non-linear regimes, it is of interest further to characterize the spatio-temporal development of ligaments as they move downstream, and also their precise physical origin.

6.1   The spatio-temporal development of ligaments

The ligament formation in the two-dimensional simulations in the work by Valluri *et al.* (2010) occurs with a remarkable regularity. In the linearly absolutely unstable regime, the dominant frequency in spectra taken from the interface height was close to the saddle-point frequency; a broader spectrum was obtained in a convectively unstable case. The results presented in this paper can in fact be integrated into this two-dimensional picture, since the formation of three-dimensional structures (waves, ligaments) is due initially to a rapidly-growing (linearized) two-dimensional wave, which subsequently excites three-dimensional nonlinear disturbances. The aim of this section is to obtain a diagnostic tool appropriate for three dimensions analogous to the spacetime plots of wave elevation in the work by Valluri *et al.* (2010). This tool should enable the observation of the co-creation of two-dimensional waves and three-dimensional structures, and provide a means of measuring the frequency with which these structures are created.

For these reasons, we track back the origin of the ligaments via the total interfacial curvature $\kappa_x(x,t)$, defined here as

$$\kappa_x(x,t) = \max_{y,z} \left(\nabla \cdot \hat{\boldsymbol{n}} \right). \tag{11}$$

This quantity is plotted in respect of simulations CH5 and CH6 (Table 3). A further parameter case is also examined, wherein $(Re, m, \mathcal{S}) = (300, 30, 0.3)$, with forcing amplitude $A_0 = 300$ and geometric parameters $(L_x, L_y, L_z) = (8.16, 1, 1)$. This simulation is referred to as CH7. The results are plotted in the (x,t) plane in Figure 15. We have also examined a further curvature-related quantity, namely $\max_{y,z} \nabla_2 \cdot (\nabla_2 \phi / |\nabla_2 \phi|)$, where $\nabla_2 = (\partial_y, \partial_z)$ denotes the gradient operator restricted to the (y,z)-plane. A spacetime plot based on this further curvature-related quantity yields a nearly-identical picture (not shown). For all three plots in Figure 15, the narrow strips in spacetime where the curvature initially develops a large magnitude can be related to the formation of interfacial waves, as is readily verified by comparison with the interfacial snapshots, either in Figure 13 for CH5, or Figure 14 for CH6. These narrow strips broaden into much wider regions of spacetime
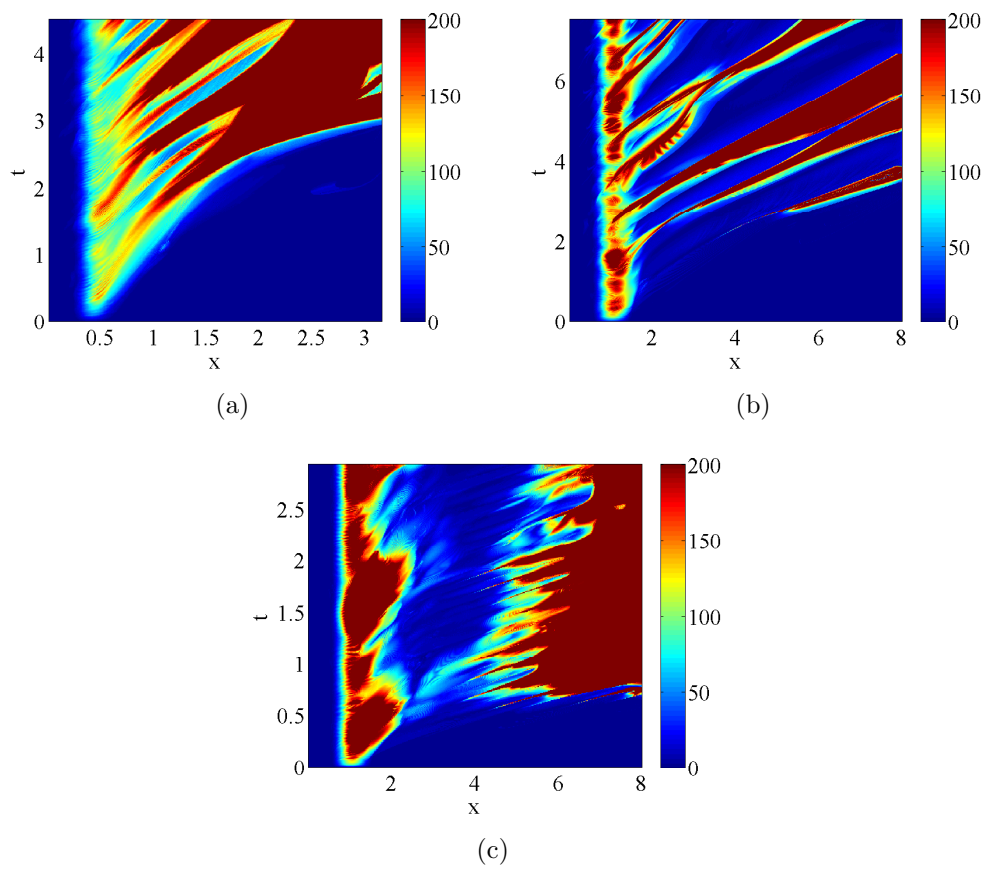
24

Figure 15: The maximum curvature in (y, z) planes versus (x, t) for Cases CH5 (a), CH6 (b), and CH7 (c).

where the curvature attains an even larger magnitude. These regions are similarly associated with with ligaments.

The snapshots in Figure 15 also highlight the regularity with which wave/ligament structures occur in all three parameter cases. These clearly defined frequencies in turn provide a very clear framework in which to connect the development of the interfacial waves to linear stability analysis. Reference is made here to two-dimensional standard linear theories for spatially localized continuous-in-time forcing (the use of two-dimensional theories has already been justified at the start of this section). These theories predict two kinds of system response (Huerre & Monkewitz, 1990; Huerre, 2000; Otto *et al.*, 2013), determined by the solution of a linearized equation for the streamfunction $\psi(x,t)$, with localized continuous-in-time forcing $\delta(x)\mathrm{e}^{-\mathrm{i}\Omega_f t}$:

$$\psi(x,t) = \frac{\mathrm{e}^{-\mathrm{i}\Omega_f t}}{2\pi} \int_{-\infty}^{\infty} \frac{\mathrm{e}^{\mathrm{i}\alpha x}}{D(\alpha,\Omega_f)}\mathrm{d}\alpha + \frac{1}{2\pi}\int_{-\infty}^{\infty} \frac{\mathrm{e}^{\mathrm{i}\alpha x - \Omega(\alpha)t}}{[\Omega(\alpha) - \Omega_f]\frac{\partial D}{\partial \Omega}\big|_{(\alpha,\Omega(\alpha))}}\mathrm{d}\alpha, \qquad (12)$$

where $D(\Omega,\alpha)$ denotes the dispersion relation obtained from the unforced normal-mode eigenvalue problem for the streamfunction $\psi(x,t)$. The two kinds of response are obtained by performing the integrals in Equation (12): the first integral is performed using the theory of residues and the second one is carried out using the saddle-point method (Huerre, 2000). The result is

$$\psi(x,t) \sim \mathrm{i}H(x)\frac{\mathrm{e}^{\mathrm{i}[\alpha^+(\Omega_f)x - \Omega_f t]}}{\frac{\partial D}{\partial \Omega}\big|_{(\alpha^+(\Omega_f),\Omega_f)}} - \mathrm{i}H(-x)\frac{\mathrm{e}^{\mathrm{i}[\alpha^-(\Omega_f)x - \Omega_f t]}}{\frac{\partial D}{\partial \Omega}\big|_{(\alpha^-(\Omega_f),\Omega_f)}}$$

$$+ \sqrt{\frac{2}{\pi}}\mathrm{e}^{-\mathrm{i}\pi/4}\left(t\frac{d^2\Omega}{d\alpha^2}\bigg|_{\alpha_0}\right)^{-1/2} \frac{\mathrm{e}^{\mathrm{i}[\alpha_0 x - \Omega(\alpha_0)t]}}{[\Omega(\alpha_0) - \Omega_f]\frac{\partial D}{\partial \Omega}\big|_{(\alpha_0,\Omega(\alpha_0))}}, \qquad t \to \infty, \quad (13)$$

where α_0 denotes the saddle point of Ω in the complex α-plane, and $\alpha^\pm(\Omega_f)$ denotes the spatial growth rates associated with downstream propagation (plus sign) and upstream propagation (minus sign). In reality, Equation (13) is a rather simplified picture of the response, and arguments based on the saddle point can be complicated by the existence of multiple saddle points, non-pinching saddles, and branch cuts in the function $\Omega(\alpha)$ (Ó Náraigh & Spelt, 2013; Juniper, 2006; Healey, 2006). However, in the cases considered in this paper, Equations (12)–(13) apply. (Of course, this statement is subject to the reservation that the present system is 3D, but see the start of this section for the arguments concerning the applicability of the 2D theory to the present system). Thus, in the absolutely unstable case, for which $\Im[\Omega(\alpha_0)] > 0$, the last term in Equation (13) dominates, and the response of the system to forcing is simply to oscillate at a natural frequency selected by the system (i.e. the saddle-point frequency). Also, the disturbance is amplified in time at a rate given by the imaginary part of the saddle-point frequency. On the other hand, for convectively unstable cases with $\Im[\Omega(\alpha_0)] < 0$, the last term in Equation (13) dies out as $t \to \infty$, meaning that only the first two terms survive, and the response of the system to forcing is therefore to act as an amplifier, whereby the system oscillates temporally at the input forcing frequency while undergoing spatial amplification both downstream and upstream from the forcing.

	x	Ω (DNS)	Ω_{r} (OS)	C/A (OS)	$\Re[\Omega(\alpha_0)]$ (OS)	$\Omega_{f,\mathrm{max}}$ (OS)
CH5	1.3	7.5 ± 0.6	7.09	A	7.08	N/A
CH6	2	5.9 ± 0.4	5.73	A	6.32	N/A
CH7	4.5	37 ± 1	32.5	C	38.8	38.3

Table 4: Frequency of ligament generation for three distinct parameter cases, together with comparisons against spatio-temporal (two-dimensional) OS theory. The frequency of the most-dangerous temporal mode in Orr–Sommerfeld analysis (Ω_{r} (OS)) is shown for comparison. For cases CH5-CH6, the spatial growth rate $-\alpha_{\mathrm{i}}(\alpha_{\mathrm{r}})$ admits no maximum away from $\alpha_{\mathrm{r}} = 0$, meaning that it is impossible to compute a maximum frequency $\Omega_{f,\mathrm{max}}$.

One may extend these arguments if a combination of forcing frequencies $\{\Omega_{f1}, \cdots, \Omega_{fn}\}$ is present. For the absolutely unstable case, the conclusion is unchanged, namely that the dominant frequency in the response is given by the saddle point. For the convectively unstable case, some further discussion is needed. Using the linearity of the small-amplitude streamfunction equation, the response in Equations (12)–(13) will consist of a sum over all forcing frequencies. In the convectively unstable case, the dominant frequency well downstream (upstream) of the forcing will be that frequency $\Omega_{f,\mathrm{max}}$ that maximizes the pertinent spatial growth rate, i.e. $\Omega_{f,\mathrm{max}}$ corresponds to the most negative spatial wave number in the set $\{\alpha_{\mathrm{i}}^{\pm}(\Omega_{f1}), \cdots, \alpha_{\mathrm{i}}^{\pm}(\Omega_{fn})\}$. This description is confirmed in numerical simulations in the absolutely unstable case (Valluri *et al.*, 2010). In those simulations, it was not possible to confirm the theory for the convective case: because the spatial location where the temporal frequencies were measured was very close to the source of the localized forcing (necessarily so because the large spatial amplification rapidly led to wave overturning), such that the most-important forcing frequency did not have enough space to be selected by the spatial amplification arising from the different frequency-dependent spatial growth rates.

We apply the theory in Equations (12)–(13) by considering the frequency of ligament formation in the cases CH5–CH7. This was measured by examining a time series $\kappa_x(x, t)$, at a fixed location x. The frequencies were extracted by eye from Figure 15 and the results were subsequently verified by a full spectral analysis of $\kappa_x(x, t)$ by carrying out Fourier transforms with respect to t at fixed x-locations. The frequencies reported in Table 4 are obtained by the spectral analysis and the error bound in the measured frequency is half the sampling frequency. The results are shown in Table 4. The results are consistent with the theory in Equations (12)–(13). For absolutely unstable parameter sets, the frequency of wave/ligament generation is governed by the saddle-point frequency. For the convectively unstable parameter set, the various theoretical frequencies are rather close, making any firm conclusion difficult, although the DNS result for the generation frequency is the closest to the forcing frequency that maximizes the spatial growth. This description of the co-evolution of waves and ligaments is further strengthened in the following section, where the mechanism for the ligament formation is examined, with due regard to the life cycle of the ligament, from its genesis in linear waves, to its ultimate fate as it is stretched and distorted by the background flow.
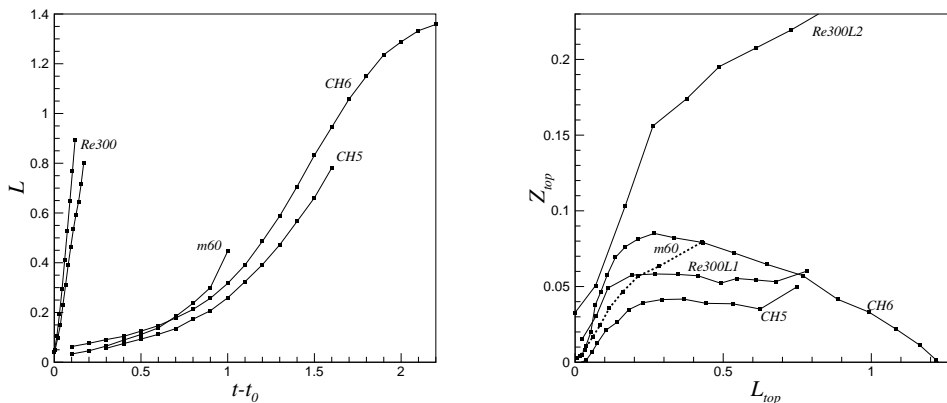
Figure 16: Ligament length versus time (a) and position of the top of the ligament tip relative to the interface above the foot (b) for various cases as indicated. In CH5 and $m = 60$, the ligaments are mostly thin sheets, whereas that traced in CH6 is a highly elongated thread. For $Re = 300$, two ligaments have been traced: one being thread-like (labelled $Re300L1$), the other tongue-like (labelled $Re300L2$). The data are shown up to the point of tearing or breakup.

6.2 Ligament kinematics

Of the late-time behaviour ligaments we first study the distance between tip and foot of ligaments in Figure 16(a). The timescale of growth is more or less the same in all cases (including varying the surface tension parameter $\mathcal{S}$ and the viscosity ratio m), with the notable exception of cases wherein the Reynolds number, Re, is varied. The fact that an increase in the value of $\mathcal{S}$ by an order of magnitude hardly affects the ligament length as a function of time is incompatible with the governing physical mechanism being the work done by tangential shear stress being converted into surface energy, as in a droplet stretched whilst pinned on a wall in shear flow (e.g. Ding *et al.* (2010)). Furthermore, the ligament dynamics argument of Marmottant & Villermaux (2004) for gas-assisted jets, when modified such that a rate of change of momentum of a ligament corresponds to the shear stress integrated over the ligament (rather than normal stress), would lead one to expect a significant dependency in Figure 16(a) on the value of m, which is not observed.

The results in Figure 16(a) suggest instead that these ligaments are elongated in a kinematic way, in line with the 'strong-flow' regime of droplet stretching in the work by Cristini *et al.* (2003). A vector $\mathbf{L}$ is advected passively approximately according to Batchelor (1967) (Chapter 3),

$$\frac{dL_i}{dt} = L_j \frac{\partial u_i}{\partial x_j}. \tag{14}$$

where it is assumed that the vector length is small compared to length scales over which $\nabla \mathbf{u}$ varies. We first observe that a unidirectional flow (over a flat interface) is independent of $\mathcal{S}$, and that the corresponding dimensionless shear rate just above the interface is hardly affected by the value of m but varies approximately linearly with the value of Re. The large discrepancy in time scale seen in Figure 16(a) for

$Re = 300$ (when compared with the other cases, which are all at $Re = 100$) can largely be explained by kinematic elongation of ligaments: after multiplying the time variable by Re, the velocity of elongation for $Re = 300$ differs only by a factor of about two from the other data.

In fact, Equation (14) explains further details of the behaviour of ligaments in these flows. Two regimes are seen in Figure 16(a): an early-time behaviour, which further inspection of our data shows to be near-exponential in time, and a near-linear regime. Although such behaviour was also observed in the two-dimensional simulations in the work by Valluri *et al.* (2010), no further analysis was offered there. In Figure 16(b), it is seen that at early times (up to the end of a near-exponential time dependency in Figure 16(a)), the relative position of the interface above the tip moves upwards relative to the interface above the ligament foot (we have found this to be caused mostly by a downwards motion of the latter, which would be expected from the foot - initially a large-amplitude wave - is drained to form part of the ligament). The largest variation in the velocity field is normal to the interface, and from Equation (14), this component of **L** is expected to increase exponentially. Subsequently, this component of **L** saturates, rendering the right-hand side of Equation (14) constant, thereby resulting in linear elongation.

7 Transition to interfacial 'turbulence'

Finally, we consider in more detail some simulation results concerning the simulation CH7 ($Re = 300, \mathcal{S} = 0.1$). The resolution $\Delta z = 1/160$ is still adequate to reproduce small-amplitude waves consistent with Orr–Sommerfeld theory, and furthermore, to produce more complicated grid-independent results at finite amplitudes. However, the timestep was reduced to 7.5×10^{-5}, such that the advective CFL number based on the inlet streamwise velocity is 0.23. Snapshots of the interface are shown at various times in Figure 17–18. The early-time $t \lesssim 0.675$ results are similar to those observed before for different parameter values: the disturbances downstream of the forcing region are largely two-dimensional, with three-dimensional perturbations superimposed on the crest of large-amplitude two-dimensional waves. These waves are stretched into sheet-like ligaments reminiscent of those seen in the case CH5 (e.g. the large three-dimensional overturned wave at $x \approx 6$, at $t = 0.75$). As the ligament is stretched by the mean flow, it 'rolls up' and is carried out of the domain. However, these events are accompanied by a violent collision on the windward side between the ligament's carrier wave and a neighbouring ligament just upstream (e.g. $t = 0.9, 0.975$). Such collisions continue indefinitely, leading to a complicated 'turbulent' interfacial structure near the outlet.

Although irregular flow behaviour is observed in prior work (Valluri *et al.*, 2010; Fuster *et al.*, 2009), its relation to a weakly-perturbed state is unclear from these studies. In fact, the transition to a highly-agitated state observed in Figure 18 for a three-dimensional system appears within a very short distance downstream from the region where waves are still of small amplitude. The basic description given above is supported by a further simple kinematic argument. For CH7, the frequency of ligament generation is five times greater than that of CH5 (see Table 4). In addition, the ligaments form only well downstream of the localized forcing (see Table 4 and
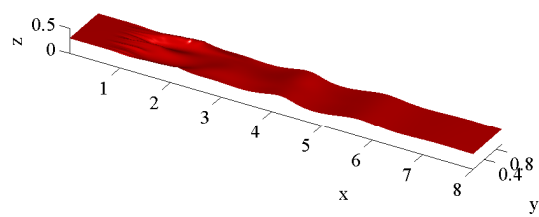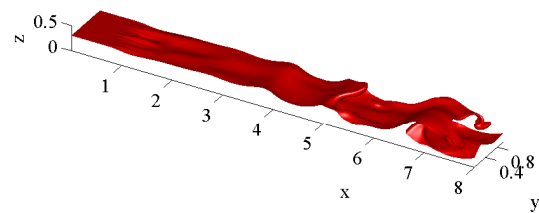
(a) $t = 0.525$
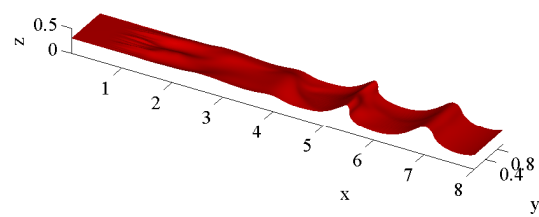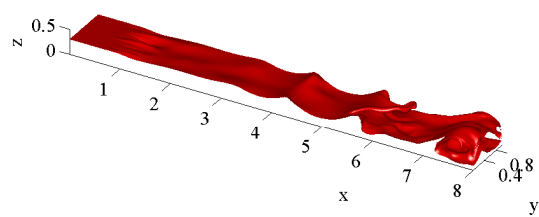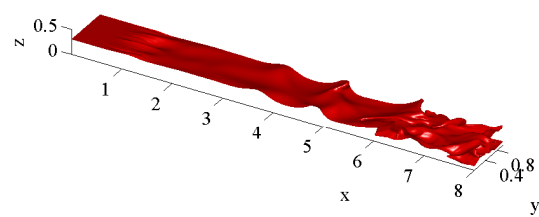
(b) $t = 0.675$
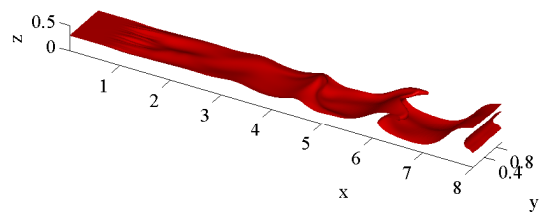
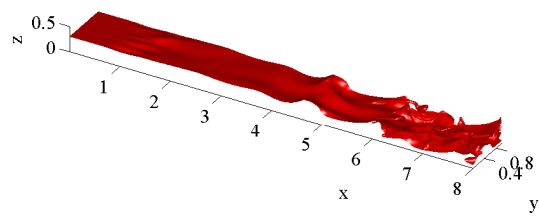(c) $t = 0.75$

(d) $t = 0.825$

Figure 17: DNS for the CH7 case ($Re = 300, \mathcal{S} = 0.1$) – interface height at various early times.
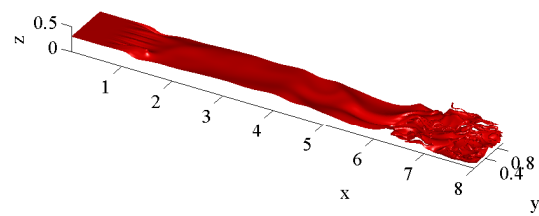
(a) $t = 0.9$

(b) $t = 0.975$

(c) $t = 1.125$

(d) $t = 1.35$

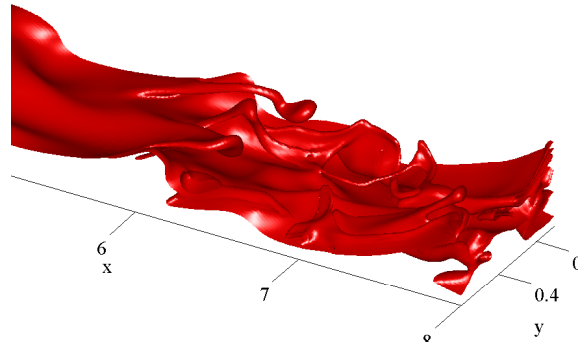Figure 18: DNS for the CH7 case ($Re = 300, \mathcal{S} = 0.1$) – interface height at later times.

Figure 19: Snapshot of the interface height at $t = 1.125$, enlarged with respect to the previous figure to show the co-existence of ligament 'sheets' and 'fingers'.

Figure 17–18). Thus, a large number of ligaments is created very rapidly in a small part of the domain. In addition, these ligaments are distorted by the mean flow, wherein the mean shear rate on the gas side is three times larger for CH7 compared to CH5 (the mean shear rate is directly proportional to the Reynolds number). Consequently, the extreme nonlinear structures in the flow are 'bunched up' and interact to form the extremely complicated structures seen at late times in Figure 18.

In Section 5 a distinction (albeit superficial) was drawn between the cases CH5 and CH6, based on the magnitude of $\mathcal{S}$ and the resulting ligament shapes: in CH5 (low surface tension), the overturning waves initially formed three-dimensional 'sheets', while for CH6, elongated ligaments were observed. For $Re = 300$, both structures are observed simultaneously (Figure 19). In certain gas-liquid systems (Marmottant & Villermaux, 2004), elongated liquid sheets (similar to those described herein) are inflated with gas from the upper layer to produce bag-like shapes that subsequently break up to produce droplets. This mechanism is typically contrasted with the scenario wherein finger-like ligaments that extend in the streamwise direction break up into droplets (Azzopardi, 2003; Marmottant & Villermaux, 2004). However, Figure 19 demonstrates that both phenomena may coexist, since both 'sheets' and elongated 'fingers' are visible therein. These numerical findings are consistent with experimental results (Lecoeur *et al.*, 2010), albeit for a a density-contrasted system.

8   Discussion and conclusions

The initial motivation for the present study was to use fully nonlinear, three-dimensional numerical simulations to identify which nonlinear mechanism should dominate beyond the point where linear theory loses validity, and by what mechanism droplets are eventually formed, as a necessary basis for a future theoretical nonlinear studies, given the diversity of types of nonlinear analysis that are available. The results for initially weakly-perturbed flows have been found to mostly follow linear theory nearly up to the point of wave overturning. For a case wherein

spanwise modes are linearly stable, a subsequent nonlinear mechanism for growth has been identified and modelled theoretically, whereby spanwise modes are enslaved by the dominant streamwise mode(s). This has also been demonstrated to occur in a case wherein spanwise modes are linearly unstable, although there the spanwise modes also eventually interact, to result in more involved nonlinear behaviour.

A further candidate route to three-dimensional instability was mooted in the introduction, namely secondary instability. In this scenario, the linearly-most-dangerous streamwise mode would stabilize at large amplitude and thereafter, a finite-amplitude unidirectional travelling wave superimposed on the base state would become the 'new' base state. This new base state could itself prove unstable to three-dimensional perturbations. Secondary instability is therefore understood as the formation of secondary waves on a nonlinear but non-overturned wavy base state, and is exemplified by the kind of Floquet analysis performed by Schmid & Henningson (2001). However, in the present system, the interfacial waves (both two- and three-dimensional) turn over and form complicated highly nonlinear structures, rendering analytic and quasi-analytic Floquet analyses around a wavy nonlinear base state impossible, and secondary instability is therefore ruled out decisively in the present context. Linear transient growth (as described in the Introduction) is also ruled out as a route to three dimensionality, as the linear phase of the observed wave growth (both two- and three-dimensional) is adequately described by asymptotic (eigenvalue) linear theory.

Regarding the flow behaviour of waves that have overturned, space-time plots of the interfacial curvature have revealed regular formation of ligaments, the frequency of which has been related to linear theory in a manner that hinges upon whether the system is absolutely or convectively unstable. The results from a parametric study of the late-time evolution of ligaments and sheets have been demonstrated to support a purely kinematic explanation of ligament stretching, rather than a dynamic, force-balance-based one, and to be related to a regime of rapid stretching of droplets in extensional flow. In a case for an elevated value of the Reynolds number, a sudden transition to an agitated, strongly chaotic regime has also been presented. This sudden transition has been discussed in the context of the increased frequency at which ligaments are formed in that case.

Finally, we comment briefly on some outstanding issues and discuss possible extensions to the current work. Given our elucidation of the weakly nonlinear mechanism that precipitates three-dimensional waves by coupling a streamwise mode to a purely spanwise mode for the subcritical case (Section 4.1), a general weakly non-linear analysis (i.e. a three-dimensional extension of the work by King & McCready (2000)), would remain a useful way forward to disentangle the precise interaction terms for the supercritical case (these are not accessible in the present 3D simulations, which merely inform the growth of various modes). That said, the range in time or space wherein such weakly nonlinear interactions dominate is clearly very limited, and the frequency at which ligaments appear is still strongly coupled to linear theory.

The simulations performed so far have involved three-dimensional channels where the extent of the channel in the spanwise direction is $L_y = 0.5, 1$, and where the results were qualitatively similar for both of these geometries. However, one may

estimate the effect of widening the channel further beyond $L_y = 1$: in this situation, a larger number of spanwise modes comes into play in linear theory, some of which will be more unstable than those present in the current simulations. Thus, in wider channels, the three-dimensional effects could become more prominent (depending of course on the choice of parameters). However, this scenario involves a mere strengthening of one of the routes to three-dimensional waves discussed in the paper (namely the direct route via spanwise linear instability), and the results in such a scenario are therefore expected to be qualitatively similar to the ones already obtained. The indirect weakly nonlinear route depends strongly on a coupling of a two-dimensional mode to purely spanwise modes, and it is expected that this route would also be modified only in a qualitative fashion by going over to wider channels.

The density-matched model simulated in this paper has been selected for a number of reasons. First, it enables one to focus uniquely on interfacial instabilities driven in the linear regime by the viscosity-contrast mechanism (Yih, 1967; Boomkamp & Miesen, 1996), thereby aiding theoretical understanding of this instability in a broader context. Also, it was motivated by our initial practical modelling concern in the removal of viscous soils in plants during cleaning and product turnover operations (Valluri *et al.*, 2010). However, it will be of compelling interest to extend this analysis to systems with a density difference, thereby widening unambiguously both the applicability of the present findings and the scope of the high-performance computing model developed in this paper.

Acknowledgements

A   Orr–Sommerfeld and Orr–Sommerfeld Squire equations

We describe here the equations and the numerical method for the 3D modal analysis that is used directly in Section 2 and that forms the basis for the transient growth calculations in Section 3. In the base state, the interface is flat ($\eta = 0$), the flow is steady and unidirectional, $v = w = 0$, $u = U_0(z)$, and the pressure is linear,

$p = (dP/dL)x$, under a negative dimensionless pressure gradient, dP/dL. The solution for the laminar velocity profile is then

$$U_0(z) = \begin{cases} U_B(z) = -\frac{Re}{2m}z^2 + Az, & 0 \le z \le h_0, \\ U_T(z) = -\frac{Re}{2}(z-1)^2 + B(z-1), & h_0 \le z \le 1 \end{cases}. \quad (15)$$

The constants A and B are determined from continuity of velocity and shear stress at the interface:

$$U_B(h_0) = U_T(h_0), \qquad mU_B'(h_0) = U_T'(h_0). \quad (16)$$

As mentioned in Sections 2–3, we study the stability of the system by subjecting the base state to a small-amplitude three-dimensional perturbation. Each flow variable is expressed as a sum of the base state and the perturbation:

$$\eta = h_0 + \epsilon\eta_0 e^{i(\alpha x + \beta y - \Omega t)}, \qquad w = \epsilon\widetilde{w}(z)e^{i(\alpha x + \beta y - \Omega t)}, \qquad \omega_z = \epsilon\widetilde{\omega}_z(z)e^{i(\alpha x + \beta y - \Omega t)},$$

$$p = \frac{dP}{dL}x + \epsilon\widetilde{p}(z)e^{i(\alpha x + \beta y - \Omega t)}. \quad (17)$$

Here ϵ is the infinitesimally small amplitude of the wave and η_0 is its phase (with $|\eta_0| = 1$). Substituting Equations (17) into the equations of motion and boundary conditions, and dropping terms that are nonlinear in the perturbed variables, we get the following system of governing equations:

$$i\alpha rRe\left[\left(\widetilde{w}_B'' - k^2\widetilde{w}_B\right)(U_B - c) - \widetilde{w}_B U_B''\right] = m\left(\widetilde{w}_B'''' - 2k^2\widetilde{w}_B'' + k^4\widetilde{w}_B\right), \quad (18a)$$

$$irRe\left[\alpha\widetilde{\omega}_{zB}(U_B - c) + \beta U_B'\widetilde{w}_B\right] = m\left(\widetilde{\omega}_{zB}'' - k^2\widetilde{\omega}_z\right), \quad (18b)$$

in the bottom phase, with $k^2 = \alpha^2 + \beta^2$, and

$$i\alpha Re\left[\left(\widetilde{w}_T'' - k^2\widetilde{w}_T\right)(U_T - c) - \widetilde{w}_T U_T''\right] = \widetilde{w}_T'''' - 2k^2\widetilde{w}_T'' + k^4\widetilde{w}_T, \quad (18c)$$

$$iRe\left[\alpha\widetilde{\omega}_{zT}(U_T - c) + \beta U_T'\widetilde{w}_T\right] = \widetilde{\omega}_{zT}'' - k^2\widetilde{\omega}_{zT}, \quad (18d)$$

in the top phase. These are supplemented with the following no-slip and no-penetration boundary conditions:

$$\widetilde{w} = \widetilde{w}' = \widetilde{\omega}_z = 0 \quad (19)$$

at the walls $z = 0$ and $z = 1$. In addition, matching conditions are prescribed at the interface $z = h_0$. In the streamwise direction, continuity of velocity and tangential stress and the jump condition in the normal stress imply the following relations:

$$\widetilde{w}_B = \widetilde{w}_T, \quad (20a)$$

$$\widetilde{w}_B' + \eta_0 U_B' = \widetilde{w}_T' + \eta_0 U_T', \qquad \eta_0 = \widetilde{w}_B/(c - U_B) = \widetilde{w}_T/(c - U_T), \quad (20b)$$

$$m\left(\widetilde{w}_B'' + k^2\widetilde{w}_B\right) = \widetilde{w}_T'' + k^2\widetilde{w}_T, \quad (20c)$$

$$i\alpha rRe\left[\widetilde{w}_B(c - U_B) + \widetilde{w}_B U_B'\right] + m\left(\widetilde{w}_B''' - 3k^2\widetilde{w}_B\right)$$

$$= i\alpha Re\left[\widetilde{w}_T'(c - U_T) + \widetilde{w}_T U_T'\right] + \left(\widetilde{w}_T''' - 3k^2\widetilde{w}_T\right) + \mathcal{S}k^4\left[\frac{\widetilde{w}_T' - \widetilde{w}_B'}{i\alpha(U_B' - U_T')}\right] = 0. \quad (20d)$$

Finally, the same physical matching conditions applied to the spanwise direction give rise to the following relations:

$$\widetilde{\omega}_{zB} + \mathrm{i}\beta U'_B \eta_0 = \widetilde{\omega}_{zT} + \mathrm{i}\beta U'_T \eta_0, \tag{20e}$$

$$m\widetilde{\omega}'_{zB} = \widetilde{\omega}_{zT}. \tag{20f}$$

Equations (18)–(20) constitute an eigenvalue problem for the velocities $(\widetilde{w}_B, \widetilde{w}_T)$ and vorticity components $(\widetilde{\omega}_{zB}, \widetilde{\omega}_{zT})$, with eigenvalue $\lambda = -\mathrm{i}\alpha c = -\mathrm{i}\omega$.

We solve Equations (18)–(20) using the Chebyshev collocation method described by Boomkamp *et al.* (1997), wherein a trial solution involving the Chebyshev polynomials $T_j(\cdot)$ is proposed in each domain:

$$\widetilde{w}_B(z) \approx \sum_{j=0}^{N_B} a_j T_j(\eta_{B1}), \qquad \widetilde{\omega}_{zB}(z) \approx \sum_{j=0}^{N_B} b_j T_j(\eta_{B2}), \tag{21a}$$

$$\widetilde{w}_T(z) \approx \sum_{j=0}^{N_T} c_j T_j(\eta_{T1}), \qquad \widetilde{\omega}_{zT}(z) \approx \sum_{j=0}^{N_T} d_j T_j(\eta_{T2}); \tag{21b}$$

this reduces the differential equations (18) to a finite-dimensional eigenvalue problem. The variables $(\eta_{B1}, \eta_{B2}, \eta_{T1}, \eta_{T2})$ are linear transformations of the z-coordinate, whose range is confined to $[-1, 1]$. The trial solution for $(\widetilde{w}_B, \widetilde{w}_T)$ is substituted into the differential equation (18) and evaluated at $(N_B - 3, N_T - 3)$ interior points; similarly, the trial solution for $(\widetilde{\omega}_{zB}, \widetilde{\omega}_{zT})$ is substituted into the differential equation (18) and evaluated at $(N_B - 1, N_T - 1)$ interior points. This gives $2(N_B + N_T) - 8$ equations in $2(N_B + N_T) + 4$ unknowns; the system is closed by evaluating the trial functions at the boundaries $z = 0$ and $z = 1$, and at the interface $z = h_0$ (12 further equations). In this way, a finite-dimensional analogue of Equations (18)–(20) is obtained:

$$\boldsymbol{A}\boldsymbol{v} = \lambda \boldsymbol{B}\boldsymbol{v}, \tag{22}$$

where $\boldsymbol{A}$ and $\boldsymbol{B}$ are $2(N_B + N_T + 2) \times 2(N_B + N_T + 2)$ complex matrices, and

$$\boldsymbol{v} = (a_0, \cdots, a_{N_B}, b_0, \cdots, b_{N_B}, c_0, \cdots, c_{N_T}, d_0, \cdots, d_{N_T})^T$$

is a complex column-valued column vector. The eigenvalue λ is obtained using a standard eigenvalue solver; the correctness of the implementation of the numerical scheme has been validated by computing the dispersion relation $\lambda(\alpha, \beta)$ for a given set of flow parameters, and comparing the result with the same dispersion relation computed by an different, independent method (Sahu & Matar, 2011); the results are identical.

References

AZZOPARDI, B. J. 2003 Drops in annular two-phase flow. *Intl J. Multiph. Flow* **23 (suppl)**, 1–53.

BARTHELET, P., CHARRU, F. & FABRE, J. 1995 Experimental study of interfacial long waves in a two-layer shear flow. *J. Fluid Mech.* **303**, 23.

BATCHELOR, G. K. 1967 *An Introduction to Fluid Dynamics*. Cambridge University Press.

BOOMKAMP, P. A. M., BOERSMA, B. J., MIESEN, R. H. M. & v. BEIJNON, G. 1997 A Chebyshev collocation method for solving two-phase flow stability problems. *J. Comp. Phys* **132**, 191.

BOOMKAMP, P. A. M. & MIESEN, R. H. M. 1996 Classification of instabilities in parallel two-phase flow. *Int. J. Multiphase Flow* **22**, 67.

BOYD, J. P. 2001 *Chebyshev and Fourier Spectral Methods*. Dover.

CRISTINI, V., GUIDO, S., ALFANI, A., BLAWZDZIEWICZ, J. & LOEWENBERG, M. 2003 Drop breakup and fragment size distribution in shear flow. *J. Rheol.* **47**, 1283–1298.

DELBENDE, I. & CHOMAZ, J.-M. 1998 Nonlinear convective/absolute instabilities in parallel two-dimensional wakes. *Phys. Fluids* **10**, 2724–2736.

DELBENDE, I., CHOMAZ, J.-M. & HUERRE, P. 1998 Absolute/convective instabilities in the Batchelor vortex: a numerical study of the linear impulse response. *J. Fluid Mech.* **355**, 229–254.

DING, H., GILANI, M. N. H. & SPELT, P. D. M. 2010 Sliding, pinch-off and detachment of a droplet on a wall in shear flow. *J. Fluid Mech.* **644**, 217–244.

DING, H., SPELT, P. D M. & SHU, C. 2007 Diffuse interface model for incompressible two-phase flows with large density ratios. *J. Comput. Phys.* **226**, 2078.

FUSTER, D., AGBAGLAH, G., JOSSERAND, C., POPINET, S. & ZALESKI, S. 2009 Numerical simulation of droplets, bubbles, and waves: state of the art. *Fluid Dyn. Res.* **41**, 065001.

GROPP, W., LUSK, E. & SKJELLUM, A. 1994 *Using MPI: portable parallel programming with the message-passing interface*. Cambridge, MA: MIT Press.

HEALEY, J. J. 2006 A new convective instability of the rotating-disk boundary layer with growth normal to the disk. *J. Fluid Mech.* **560**, 279.

HUERRE, P. 2000 Open shear flow instabilities. In *Perspectives in Fluid Mechanics* (ed. G. K. Batchelor, H. K. Moffatt & M. G. Worster). Cambridge.

HUERRE, P. & MONKEWITZ, P. A. 1990 Local and global instability in spatially developing flows. *Ann. Rev. Fluid Mech.* **22**, 473–537.

JUNIPER, M. P. 2006 The effect of confinement on the stability of two-dimensional shear flows. *J. Fluid Mech.* **565**, 171.

KING, M.R. & MCCREADY, M.J. 2000 Weakly nonlinear simulation of planar stratified flows. *Phys. Fluids* **12**, 92–102.

LECOEUR, N., HALE, C. P., SPELT, P. D. M. & HEWITT, G. F. 2010 Visualization of droplet entrainment in turbulent stratified pipe flow. In *7th International Conference on Multiphase Flow ICMF 2010*.

MARMOTTANT, P. & VILLERMAUX, E. 2004 On spray formation. *J. Fluid Mech.* **498**, 72–111.

MELAND, R., GRAN, I.R., OLSEN, R. & MUNKEJORD, S. T. 2007 Reduction of parasitic currents in level-set calculations with a consistent discretization of the surface-tension force for the csf model. In *Proceedings, 16th Australasian Fluid Mechanics Conference*.

VAN NOORDEN, T. L., BOOMKAMP, P. A. M., KNAPP, M. C. & VERHEGGEN, T. M. M. 1998 Transient growth in parallel two-phase flow: Analogies and differences with single-phase flow. *Phys. Fluids* **10**, 2099.

OTTO, THOMAS, ROSSI, MAURICE & BOECK, THOMAS 2013 Viscous instability of a sheared liquid-gas interface: Dependence on fluid properties and basic velocity profile. *Phys. Fluids* **25**, 032103.

RUSSO, G. & SMEREKA, P. 2000 A remark on computing distance functions. *J Compu Phys* **163**, 51.

SAHU, K. & MATAR, O. K. 2011 Three-dimensional convective and absolute instabilities in pressure-driven two-layer channel flow. *Int. J. Multiphase Flow* **37**, 987.

SCARDOVELLI, R. & ZALESKI, S. 1999 Direct numerical simulation of free-surface and interfacial flow. *Annu. Rev. Fluid Mech.* **31**, 567.

SCHMID, P. J. & HENNINGSON, D. S. 2001 *Stability and Transition in Shear Flows*. New York: Springer.

SCOTT, D. M., NÁRAIGH, L. Ó, BETHUNE, I., VALLURI, P. & SPELT, P. D. M. 2013*a* Performance enhancement and optimization of the TPLS and DIM two-phase flow solvers. *Tech. Rep.*. Edinburgh Parallel Computing Centre.

SCOTT, D. M., NÁRAIGH, L. Ó, BETHUNE, I., VALLURI, P. & SPELT, P. D. M. 2013*b* TPLS: High resolution direct numerical simulation (DNS) of two-phase flows. http://sourceforge.net/projects/tpls/.

SUSSMAN, M. & FATEMI, E. 1998 An efficient, interface-preserving level set redistancing algorithm and its application to interfacial incompressible flow. *SIAM Journal on Scientific Computing* **24**, 1165–1191.

Ó NÁRAIGH, L. & SPELT, P. D. M. 2013 An analytical connection between temporal and spatio-temporal growth rates in linear stability analysis. *Proc R Soc A* **469**, 20130171.

Ó NÁRAIGH, L., SPELT, P. D. M. & SHAW, S. J. 2013 Absolute linear instability in laminar and turbulent gas/liquid two-layer channel flow. *J. Fluid Mech.* **714**, 24.

VALLURI, P., SPELT, P.D.M., LAWRENCE, C.J. & HEWITT, G.F. 2007 Numerical simulation of the onset of slug initiation in laminar horizontal channel flow. *Int. J. Multiphase Flow* **34**, 206.

VALLURI, P., Ó NÁRAIGH, L., DING, H. & SPELT, P. D. M. 2010 Linear and nonlinear spatio-temporal instability in laminar two-layer flows. *J. Fluid Mech.* **656**, 458–480.

YECKO, P. & ZALESKI, S. 2005 Transient growth in two-phase mixing layers. *J. Fluid Mech.* **528**, 43.

YECKO, P., ZALESKI, S. & FULLANA, J.-M. 2002 Viscous modes in two-phase mixing layers. *Phys. Fluids* **14**, 4115.

YIANTSIOS, S. G. & HIGGINS, B. G. 1988 Linear stability of plane Poiseuile flow of two superposed fluids. *Phys. Fluids* **31**, 3225.

YIH, C. S. 1967 Instability due to viscosity stratification. *J. Fluid Mech.* **27**, 337.